RSC Advances

PAPER

View Article Online
View Journal | View Issue

Cite this: *RSC Adv.*, 2020, **10**, 44551

Heterogeneous activation of persulfate by $ZnCo_xFe_{2-x}O_4$ loaded on rice hull carbon for degrading bisphenol A

Yirui Shu,[ab] Pan Zhang,[ab] Yanjun Zhong,[ab] Xiangyang Xu,[c] Genkuan Ren,[d] Wei Wang,[ab] Hengli Xiang,[ab] Zhiye Zhang,[ab] Xiushan Yang *[ab] and Xinlong Wang[ab]

A new low-cost composite of $ZnCo_xFe_{2-x}O_4$ loaded on rice hull carbon ($ZnCo_xFe_{2-x}O_4$-RHC) was synthesized *via* waste ferrous sulfate (the industrial waste produced in the process of producing titanium dioxide) and rice hull as raw materials, which was applied for the degradation of bisphenol A (BPA) by heterogeneous activated peroxodisulfate (PS). A series of characterizations including XRD, SEM, FTIR, and BET analysis were carried out to analyze the structure and morphology of the materials. It is confirmed that the $ZnCo_xFe_{2-x}O_4$-RHC composites show better catalytic activity and performance than other control samples, which can be attributed to the synergistic effect of Fe and Co, $ZnCo_xFe_{2-x}O_4$ and RHC based on these analyses. The degradation rate of BPA by $ZnCo_{1.3}Fe_{0.7}O_4$-50%RHC reached 100% within 15 min, and it can still maintain good catalytic efficiency after 5 cycles. ESR test and XPS results showed that free radical and non-free radical processes were involved in BPA degradation. These findings offer a novel, low cost and simple strategy for rational design and modulation of catalysts for the industrial degradation of organic pollutants, and provide a new idea for the utilization of waste ferrous sulphate in titanium dioxide industry.

Received 17th October 2020
Accepted 25th November 2020

DOI: 10.1039/d0ra08852h

rsc.li/rsc-advances

1 Introduction

Bisphenol A (BPA), also known as diphenolic propane, is an important raw material used in the manufacture of polycarbonate plastics and epoxy resins, which widely exists in industrial wastewater.[1] As a typical endocrine disruptor, BPA can mimic and interfere with the secretion of endogenous hormones, hinder the hormone's function, interfere with the hormone balance in the human body, and thus affect the endocrine, nerve, immune and reproductive systems of humans and animals, causing great harm to human health.[2,3] In addition, BPA is not biodegradable and highly resistant to chemical degradation.[4] Therefore, it is crucial to develop a cost-effective, low-consumption, green treatment technology to remove BPA in waste water.

In recent years, among the multiple technologies for removing BPA, the emerging persulfate oxidation technology based on sulfate radicals ($SO_4^{\bullet-}$) has attracted more and more attention.[5] As a kind of strong oxidant, the sulfate radical degrades organic pollutants in the system remarkably. Compared with the traditional advanced oxidation method based on hydroxyl radical ($^{\bullet}OH$), the use of $SO_4^{\bullet-}$ has a number of advantages, such as higher oxidation potential ($SO_4^{\bullet-}$, E^{θ} = 2.5–3.1 V; $^{\bullet}OH$, E^{θ} = 1.8–2.7 V),[6] higher selectivity and efficiency for organic pollutants with unsaturated bonds or aromatic rings, wider pH range (pH = 2–8), longer half-life.[7] Persulfate oxidation technology can activate $K_2S_2O_8$ (PS) through heat, ultraviolet light and transition metals (such as Fe^{2+}, Cu^{2+}, Co^{2+}, Ag^{+}) to form sulfate radicals ($SO_4^{\bullet-}$).[8–10] The use of transition metal ions requires lower activation energy than other external energy. However, it is difficult for transitional ions to recover and may cause secondary pollution. Therefore, it is of great significance to choose an activating agent for PS that can improve the recycling rate and can be magnetically separated.

Spinel ferrite [AB_2O_4 (A = Mn^{2+}, Co^{2+}, Ni^{2+}, Zn^{2+}, *etc.* B = Fe^{3+})] is a class of important functional materials because of their unique electromagnetic, optical and catalytic properties, stable chemical properties, and excellent magnetic properties. Spinel zinc ferrite ($ZnFe_2O_4$) has attracted wide attention due to its low cost, free of precious or carcinogenic metals, and environmentally friendly.[11] The synthesis methods of $ZnFe_2O_4$ mainly include solid phase method,[12] co-precipitation method,[13] hydrothermal method,[14] sol–gel method[15] and so on. Among them, the solid phase process is a simple and effective method because of operation to easy, environmentally friendly, low cost, short time, and suitable for industrialization.

[a]School of Chemical Engineering, Sichuan University, Chengdu 610065, P R China
[b]Engineering Research Center of Comprehensive Utilization and Clean Processing of Phosphorus Resources, Ministry of Education, School of Chemical Engineering, Sichuan University, Chengdu 610065, PR China. E-mail: yangxiushan3@163.com
[c]Suntime Environmental Remediation Co., Ltd, Changzhou 213000, P R China
[d]College of Chemistry and Chemical Engineering, Yibin University, Yibin 64000, P R China

The current reported studies for the synthesis of $ZnFe_2O_4$ by solid phase method usually take analytically or chemically pure ferrous sulfate as raw material.[16–18] Due to the process of producing titanium dioxide by sulfuric acid method, about 7 million tons of ferrous sulfate waste was produced in 2018, and it increases at a rate of more than 10% with the increasing demand for titanium dioxide year by year.[19–21] Nowadays most of waste ferrous sulphate is still disposed as solid waste.[22] Such vast amount of piled waste ferrous sulphate not only occupies the farm land but also causes serious pollution to the surrounding environment, and causes a great waste of renewable resources. This left us open to thinking that whether the waste ferrous sulphate could be adopted as raw materials to obtain $ZnFe_2O_4$ *via* facile solid state method, thus to realize the resource utilization of waste, and further reduce the cost of preparing $ZnFe_2O_4$. It is worth noting that the $ZnFe_2O_4$ nanoparticles prepared by the solid phase method are peculiarly prone to aggregate, which result in reduced active sites and unfavourable catalytic property.[23] On the one hand, this can be improved by Co doping because of the excellent catalytic activity of Co. Zhong *et al.*[24] confirmed that Co-doped bismuth ferrite increased the degradation rate of levofloxacin by 3.52 times compared with undoped BFO. Zhang *et al.*[25] found that Co doping $ZnFe_2O_4$ have abundant oxygen vacancy, which can rapidly activate persulfate to remove organic pollutants. In addition, due to the synergistic effect of Zn and Co, the metal ion leaching rate of Co-doped zinc ferrite nanomaterials is reduced.[26] On the other hand, the composite of ferrite nanoparticles and carbon matrix (graphene, carbon nanotubes, *et al.*) can deliver enhanced catalytic activity compared with ferrite nanoparticles, profiting from the inhibition of agglomeration by carbon matrix. It is important to choose a cheap carbon matrix from a practical industrial applications view point. For the past few years, rice hull carbon, which is a common food by-product, has been widely studied as biomass carbon source applied in many fields owing to the source cheap and sustainable.[27] The derived rice hull carbon (RHC) has the feature of large specific surface area, strong adsorption capacity, and fast conduction rate, which can raise synergistic effect between ferrite and RHC, leading to higher catalytic activity of the ferrite/RHC composite.[28]

In this study, we designed and prepared a new composite of cobalt doped zinc ferrite loaded on rice hull carbon ($ZnCo_x$-$Fe_{2-x}O_4$-RHC), *via* one-step solid phase method using waste by-product ferrous sulfate as iron source and rice hull as carbon source. The composite shows enhanced activity and property when used as a catalyst for bisphenol A degradation in persulfate system. The synthetic and degradation mechanisms and degrading BPA process were studied, the degradation conditions were optimized, and the reaction kinetics and cyclic stability of the composite were investigated systematically. This research put forward a thinking of "using waste to treat waste", which not only provides an efficient and environmentally friendly way to degrade BPA, but also expands the resource utilization of waste by-product ferrous sulfate, and thus achieve good economic and environmental benefits.

2 Experimental section

2.1. Materials

Waste by-product ferrous sulphate from Panzhihua Iron and Steel Group Co. Ltd (Sichuan, China). Rice husks are taken from Sichuan agricultural production base (Sichuan, China). Bisphenol A($C_{15}H_{16}O_2$) was purchased from Aladdin Reagent Co. Ltd. Pyrite (FeS_2) purchased from Beijing Hawke Technology Co. Ltd. Cobalt sulfate ($CoSO_4 \cdot 7H_2O$), zinc sulfate($ZnSO_4 \cdot 7H_2O$), potassium peroxosulfate ($K_2S_2O_8$), sodium hydroxide (NaOH), hydrochloric acid (HCl), ethanol (C_2H_6O, EtOH) were purchased from Chengdu Kelong Chemical Reagents Co. Ltd. *tert*-Butanol ($C_4H_{10}O$, TBA), 5,5-dimethyl-1-pyrroline-*N*-oxide (DMPO), 2,2,6,6-tetramethyl (TEMP), *p*-benzoquinone (BQ), potassium chloride (KCl), potassium nitrate (KNO_3), potassium carbonate ($KHCO_3$), potassium dihydrogen phosphate (KH_2PO_4) were purchased from Chengdu Jinshan Chemical Reagent Co. Ltd. Furfuryl alcohol ($C_5H_6O_2$, FFA) was purchased from Makerlin Biochemical Co. Ltd. All the solutions were prepared using deionized water.

2.2. Preparation of catalyst

Rice husk is washed with deionized water for several times and put them in a dry place to dry naturally. The dried rice husks are put into a ball mill and ground for 1 h at a rotational speed of 500 rpm. Then, rice husk powder is put into a tubular furnace and calcines at 600 °C for 120 min under the protection of N_2 atmosphere to obtain RHC. The cooled RHC is added to 3 M NaOH and stirrs continuously for 12 h to remove the silicon dioxide in the rice hull. The rice hull after desilication is washed many times in deionized water until it becomes neutral. Then, it is added to a solution of dilute hydrochloric acid and stirs

Table 1 Abbreviation for sample corresponding to the cobalt molar ratios in the course of synthesis (Zn/Co/Fe)

Co molar ratios (x)	$x = 0$	$x = 0.7$	$x = 1.3$	$x = 1.6$	$x = 2$
$ZnCo_xFe_{2-x}O_4$	$ZnFe_2O_4$	$ZnCo_{0.7}Fe_{1.3}O_4$	$ZnCo_{1.3}Fe_{0.7}O_4$	$ZnCo_{1.6}Fe_{0.4}O_4$	$ZnCo_2O_4$

Table 2 Abbreviation for sample corresponding to the RHC mass ratios

RHC mass ratios (y wt%)	$y = 0$	$y = 20$	$y = 40$	$y = 50$	$y = 70$
$ZnCo_{1.3}Fe_{0.7}O_4$-y%RHC	$ZnCo_{1.3}Fe_{0.7}O_4$	$ZnCo_{1.3}Fe_{0.7}O_4$-20%RHC	$ZnCo_{1.3}Fe_{0.7}O_4$-40%RHC	$ZnCo_{1.3}Fe_{0.7}O_4$-50%RHC	$ZnCo_{1.3}Fe_{0.7}O_4$-70%RHC

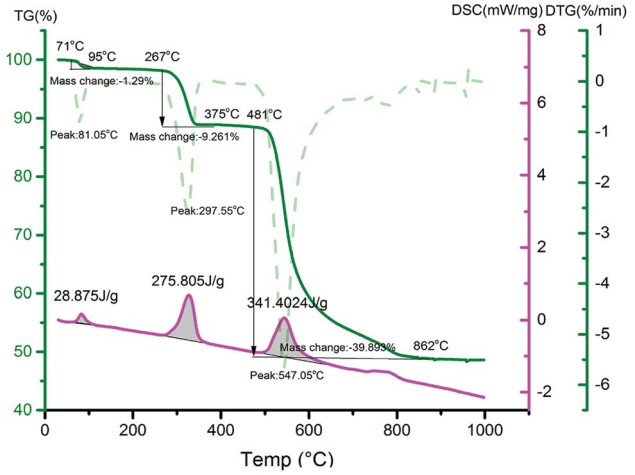

Fig. 1 TG-DSC of the obtained mixtures by mixing zinc sulfate, cobalt sulfate, waste ferrous sulfate and pyrite in a molar ratio of 4 : 4 : 3.5 : 1.

continuously for 3 h to remove the metal oxides. Washing with deionized water several times until neutral, and then dry at 50 °C for 3 h. Store in a dryer for later use.

Using pyrite as the reducing agent and waste ferrous sulfate as the iron source, the $ZnSO_4 \cdot 7H_2O$, the waste ferrous sulfate and pyrite are weighed by a certain molar ratio, and dried at 100 °C for 5 h. Then, Co molar ratios ($x = 0$, 0.7, 1.3, 1.6 and 2) (Table 1) and RHC mass ratios ($y = 0$, 20, 40, 50 and 70 wt%) (Table 2) were add into the mixture, and ball milled in a ball mill of 500 rpm for 2 hour. The mixture after homogenization was put into a tube furnace and calcined at 550 °C for 90 min under a protective atmosphere to synthesize $ZnCo_xFe_{2-x}O_4$-y wt% RHC composite. Following cooling to room temperature, wash with deionized water and absolute ethanol 5 times to remove impurities. Finally, it was dried in a freeze dryer for 24 hours.

2.3. Characterization of catalyst

Phase analysis of the catalyst is carried out using an X-ray diffractometer (XRD, Empyrean, PANalytical) at CuK ray (λ = 0.15401 nm), working current 300 mA, working voltage 40 kV, scanning speed 0.02° s^{-1}, scanning range 5–80°. Model JSM-5900LV SEM-EDX is used to analyze the surface morphology and element composition of the samples. Model XSAM800 XPS (Kratos, UK) is used to study the surface composition of the sample. The morphology of the samples is observed by JEOL JEM-12100 transmission electron microscope (TEM). The surface properties of the samples are identified by Andor SR-500I Raman spectrum (RM) and Nicolet IS10 Fourier Transform spectrum (FTIR). The reaction mechanism of the mixed materials and the thermal stability of the samples are analyzed by TG-DSC (STA 449F3, Germany). N_2 adsorption and desorption data are obtained by Mike 2460 Brunauer–Emmet–Teller technique (BET). DMPO and TEMP are used as trapping agents to analyze the free radicals generated by the reaction using electron paramagnetic resonance (ESR, JEOL JES-FA200). The Zn, Fe and Co ions released from the catalyst are detected by a plasma spectrometer (ICP-OES, Shimadzu, Japan).

2.4. Degradation experiments

The degradation process of BPA is conducted in a beaker followed by stirring at room temperature. At the same time, all experiments are carried out by adding 200 mL of BPA solution (20 mg L^{-1}), $K_2S_2O_8$ (molar ratio of $K_2S_2O_8$/biphenol A is 42.23), $ZnCo_xFe_{2-x}O_4$-y wt% RHC catalyst (0.75 g L^{-1}) to a 250 mL beaker, and the mixing paddle stirs the mixture at 400 rpm to start the catalytic degradation reaction. At each predetermined time interval (0, 3, 5, 10, 15, 20, and 30 minutes), 10 mL of the supernatant is taken out and $Na_2S_2O_3$ solution (0.5 M) is added into to the supernatant to prevent further BPA degradation. After that, the solution is centrifuged at high speed for 5 min in a centrifuge, and takes the supernatant concentration to be measured. By adding NaOH (0.1 M) and H_2SO_4 (0.1 M) to adjust pH to 2, 5, 7, 9 and 11, the effect of pH value on degradation experiment is tested. Cl^-, $H_2PO_4^-$, HCO_3^-, NO_3^- are added to the solution to explore the effect of anions on catalytic oxidation of BPA. *tert*-Butyl alcohol (TBA), ethanol (EtOH), *p*-benzoquinone (BQ) and furfuryl alcohol (FFA) are used as scavengers for $SO_4^{\cdot-}$, $^{\cdot}OH$, $^1O_2$ and $O_2^{\cdot-}$. The molar ratio of TBA to PS, EtOH to

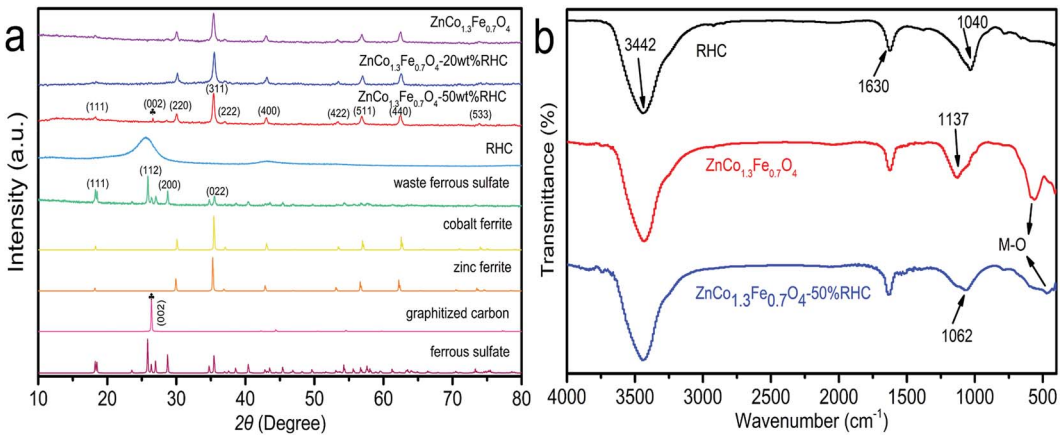

Fig. 2 The XRD patterns (a), FTIR spectra (b) of samples.

PS, BQ to PS and FFA to PS are set as 1000, 1000, 600, and 600 respectively to study the free radicals in the catalytic systems. BPA concentrations are measured at 277 nm with an ultraviolet spectrophotometer (V-5800).

3 Results and discussions

3.1. Synthesis and characterization of Zn,Co,Fe-RHC composites

The TG-DSC was used to analyze the formation mechanism of $ZnCoFeO_4$ synthesized by solid phase reduction. As shown in Fig. 1, under the protection of nitrogen, the thermal decomposition of raw materials is divided into three processes. The first stage is at the temperature range between 71 and 95 °C, with a mass loss of 1.29% due to the loss of adsorbed water on the surface of raw materials. In the second stage of 267–375 °C, the mass loss is 9.26%, which is due to the loss of crystal water in waste by-product, the loss of crystal water in zinc sulfate and cobalt sulfate. The third stage is from 481 °C to 862 °C, with a mass loss of 39.89% due to the reaction of the feedstocks with each other and the release of sulfur dioxide gas. It can be inferred that $ZnCoFeO_4$ is synthesized through the following reactions (eqn (1)–(4)):

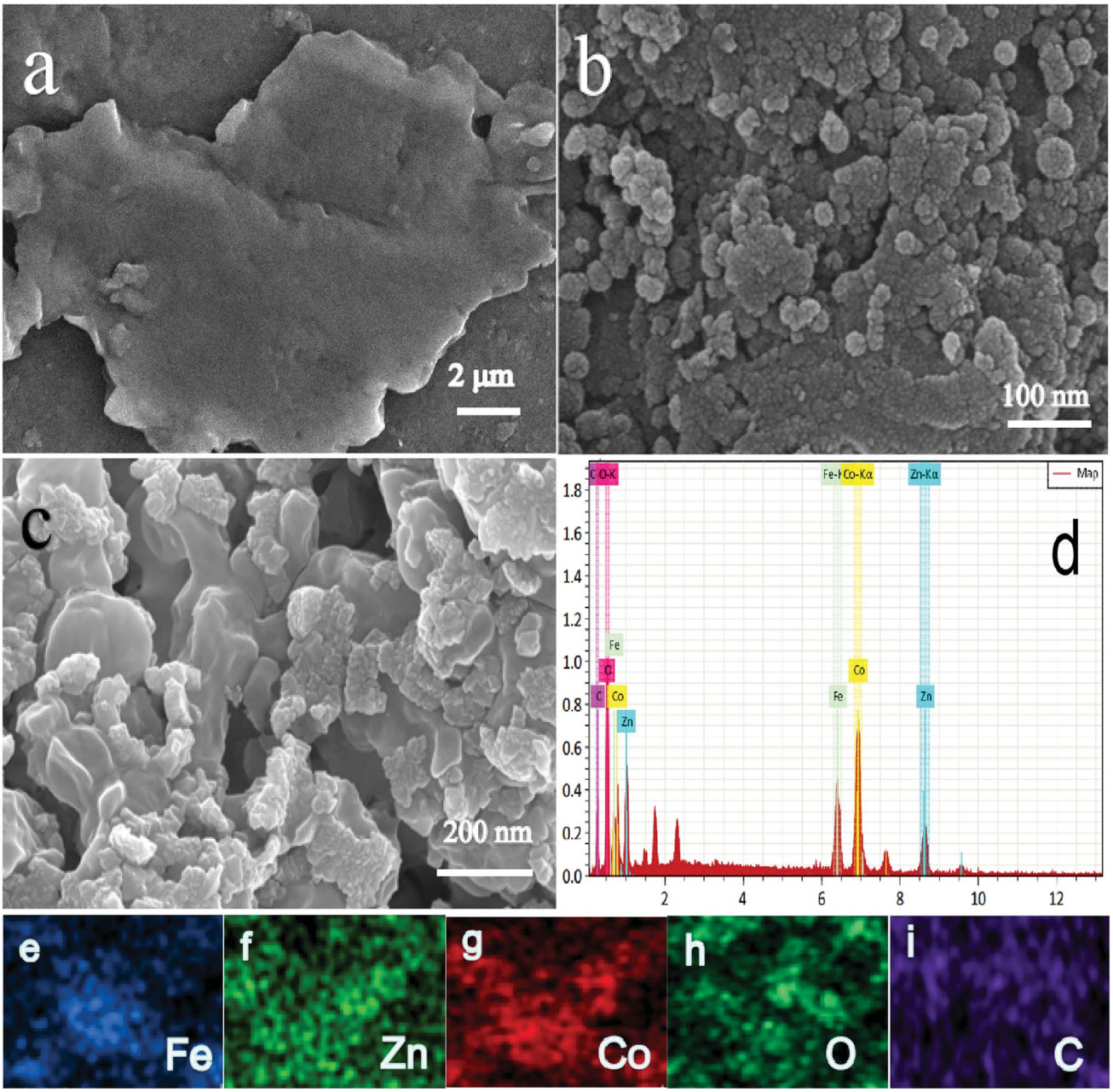

Fig. 3 SEM images of RHC (a), $ZnCo_{1.3}Fe_{0.7}O_4$ (b), $ZnCo_{1.3}Fe_{0.7}O_4$-50%RHC (c). Energy dispersive X-ray spectroscopy (EDS) patterns of $ZnCo_{1.3}Fe_{0.7}O_4$-50%RHC (d). EDS elemental mapping of Fe (e), Zn (f), Co (g), O (h) and C (i).

$$ZnSO_4 \cdot 7H_2O \rightarrow ZnSO_4 + 7H_2O(g) \quad (1)$$

$$FeSO_4 \cdot H_2O \rightarrow FeSO_4 + H_2O(g) \quad (2)$$

$$CoSO_4 \cdot 7H_2O \rightarrow CoSO_4 + 7H_2O(g) \quad (3)$$

$$2FeSO_4 + 3CoSO_4 + 3ZnSO_4 + FeS_2 \rightarrow 3ZnCoFeO_4 + 10SO_2 \quad (4)$$

Fig. 2a shows the XRD patterns of the waste ferrous sulfate, $ZnCo_{1.3}Fe_{0.7}O_4$, $ZnCo_{1.3}Fe_{0.7}O_4$-20%RHC, $ZnCo_{1.3}Fe_{0.7}O_4$-50% RHC and RHC. It can be seen that the XRD pattern of the waste ferrous sulfate is basically consistent with the standard pattern of $FeSO_4 \cdot H_2O$ (JCPDS Card No. 81-0019), indicating that the main component of the purified ferrous sulfate is $FeSO_4 \cdot H_2O$. From the XRD patterns of $ZnCo_{1.3}Fe_{0.7}O_4$, $ZnCo_{1.3}Fe_{0.7}O_4$-20% RHC and $ZnCo_{1.3}Fe_{0.7}O_4$-50%RHC, it can be observed that the 2θ values of the diffraction peaks are 18.16°, 30.05°, 35.43°, 36.94°, 42.97°, 56.91° and 62.43°, corresponding to the crystal planes (111), (220), (311), (222), (400), (511) and (440) respectively for the as-obtained samples, which are in agreement well with the standard characteristic peaks for the cubic spinel ferrites with the conventional formula $[Fe^{3+}]_A[M^{2+}Fe^{3+}]_BO_4$ as a reference standard for $ZnFe_2O_4$ (JCPDS Card No. 77-0011) and $CoFe_2O_4$ (JCPDS Card No. 22-1086).[29] RHC has a broad peak at 25.23°, which is indicative of amorphous carbon. The (002) crystal plane appeared in the XRD pattern of $ZnCo_{1.3}Fe_{0.7}O_4$-50%RHC (JCPDS Card No. 41-1487), indicating that rice husk carbon was successfully doped into $ZnCo_{1.3}Fe_{0.7}O_4$.[30] The (002) crystal plane did not appear in the XRD pattern of $ZnCo_{1.3}Fe_{0.7}O_4$-20%RHC because the doped biochar content is less, and the intensity of the diffraction peak is weak, which is covered by the strong peak of $ZnCo_{1.3}Fe_{0.7}O_4$. These XRD results indicate that $ZnCo_{1.3}Fe_{0.7}O_4$ nanoparticles were successfully interspersed on the rice husk carbon substrate.

The FTIR spectra of RHC, $ZnCo_{1.3}Fe_{0.7}O_4$ and $ZnCo_{1.3}Fe_{0.7}O_4$-50%RHC are shown in Fig. 2b. The absorption peaks of 1040, 1630 and 3442 cm^{-1} in the RHC spectrum can be attributed to C–O–C stretching vibration, C=O stretching vibration and O–H stretching vibration in water molecules, respectively.[31] Comparing with the spectra of RHC and $ZnCo_{1.3}Fe_{0.7}O_4$-50% RHC. We can observe the peaks corresponding to oxygen-containing functional groups in RHC with a slight shift for some of them, which indicates that RHC has been supported well on the $ZnCo_{1.3}Fe_{0.7}O_4$ in $ZnCo_{1.3}Fe_{0.7}O_4$-50%RHC. Besides, the absorption peak of 571 cm^{-1} observed in the spectrum of $ZnCo_{1.3}Fe_{0.7}O_4$ can be attributed to the stretching vibration of Zn^{2+}–O^{2-} while the absorption peak of 413 cm^{-1} can be attributed to the stretching vibration of M^{3+}–O^{2-} (Co^{3+}–O^{2-}, Fe^{3+}–O^{2-}) in typical spinel ferrite.[32] In the FTIR spectrum of $ZnCo_{1.3}Fe_{0.7}O_4$-50%RHC, the peak value of metallic bond (M–O) corresponding to $ZnCo_{1.3}Fe_{0.7}O_4$ varies. This means that $ZnCo_{1.3}Fe_{0.7}O_4$-50%RHC is not a simple mixture of $ZnCo_{1.3}Fe_{0.7}O_4$ and RHC.

Fig. 3a–c are SEM images of RHC, $ZnCo_{1.3}Fe_{0.7}O_4$ and $ZnCo_{1.3}Fe_{0.7}O_4$-50%RHC, respectively. It can be seen from Fig. 3a that the RHC has a smooth surface and a huge sheet structure. The $ZnCo_{1.3}Fe_{0.7}O_4$ shows nano-structure with uniform spherical particles, and it occurs agglomeration of nanoparticles caused by electrostatic attraction and van der

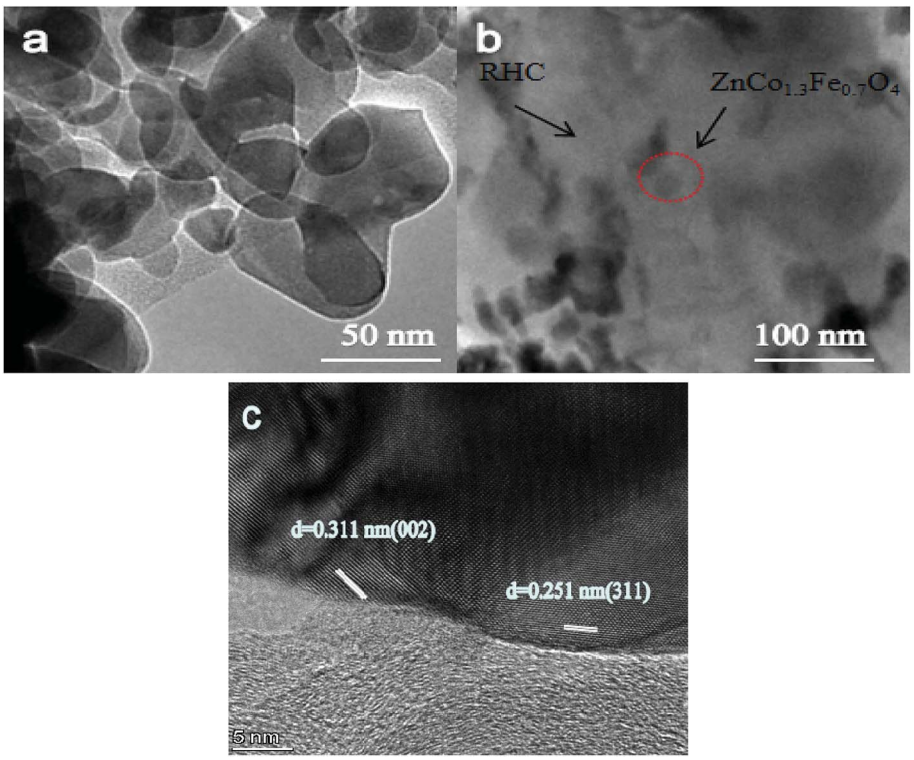

Fig. 4 TEM images of $ZnCo_{1.3}Fe_{0.7}O$ (a), $ZnCo_{1.3}Fe_{0.7}O_4$-50%RHC (b). HRTEM images of $ZnCo_{1.3}Fe_{0.7}O_4$-50%RHC (c).

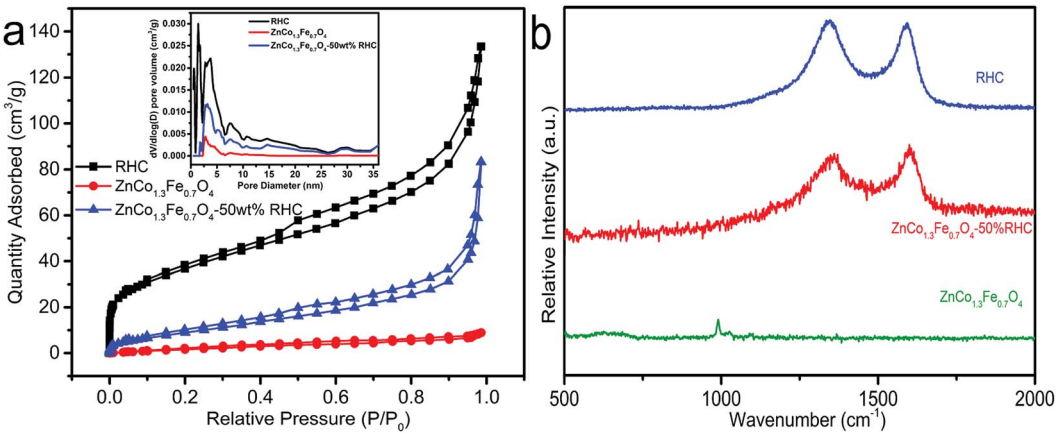

Fig. 5 N_2 adsorption–desorption isotherms (a), Raman spectra (b).

Waals force. From Fig. 3c, the $ZnCo_{1.3}Fe_{0.7}O_4$ nanoparticles are interspersed in the RHC, which alleviates the agglomeration phenomenon to a certain extent. The EDX spectrum result shown in Fig. 3d indicates that the prepared sample is composed of Fe, Zn, O, Co and C. The element map confirms that the distribution of Zn, Co, Fe, O and C is relatively uniform, which is beneficial to enhance the catalytic activity.

Fig. 4a and b display the TEM micrographs of $ZnCo_{1.3}Fe_{0.7}O_4$-50%RHC and $ZnCo_{1.3}Fe_{0.7}O_4$ composites. $ZnCo_{1.3}Fe_{0.7}O_4$ shows serious aggregation state in Fig. 4a, which is consistent

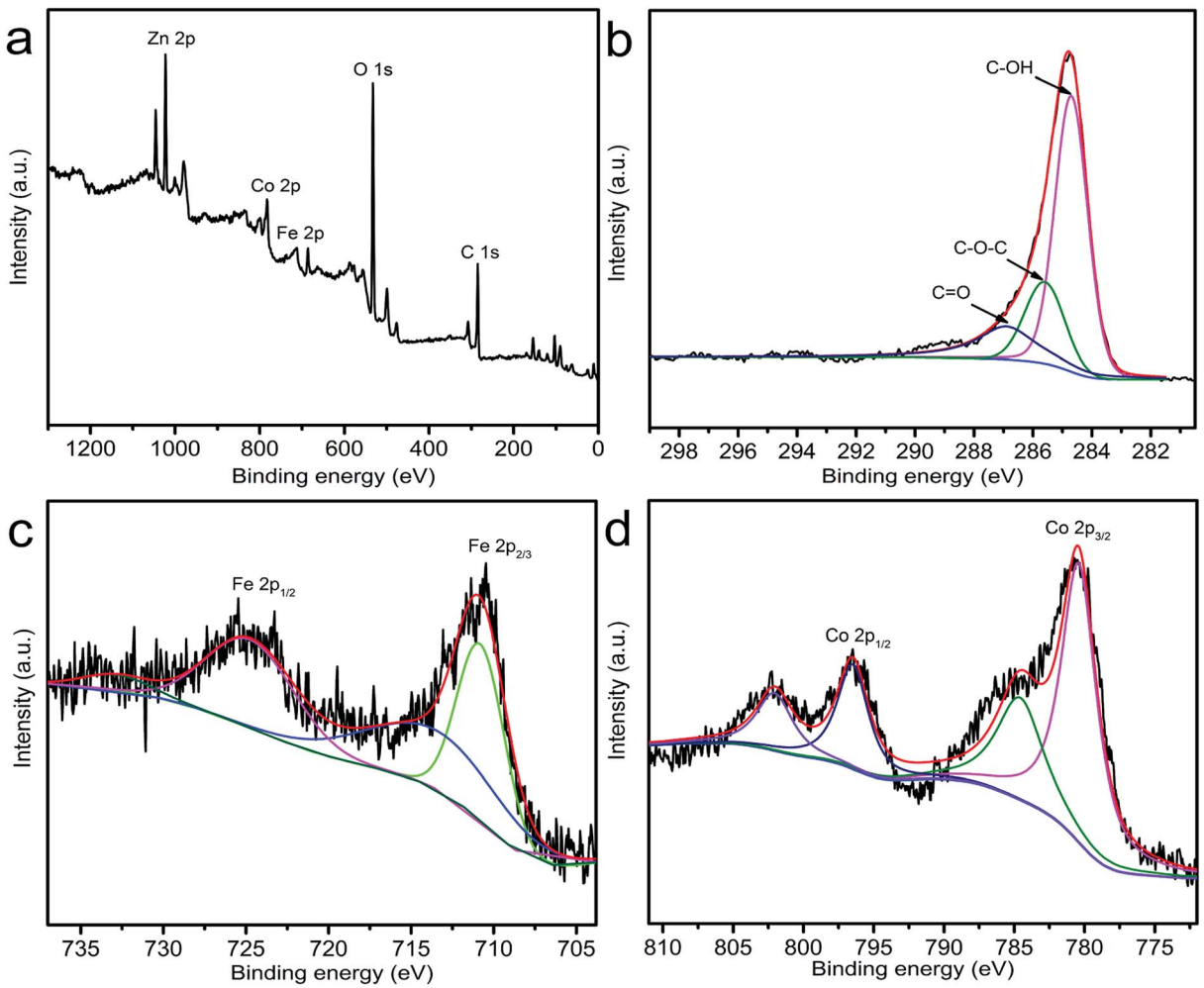

Fig. 6 XPS spectrum of wide-scan (a), C 1s (b), Fe 2p (c) and Co 2p (d) of $ZnCo_{1.3}Fe_{0.7}O_4$-50%RHC composites.

with SEM results. In addition, the $ZnCo_{1.3}Fe_{0.7}O_4$ nanoparticles (Fig. 4b) are embedded in the biological carbon layer, indicating that the RHC acts as a carrier material and disperses $ZnCo_{1.3}Fe_{0.7}O_4$ nanoparticles. It can be seen from Fig. 4c that the spacing of (311) crystal planes corresponding to $ZnCo_{1.3}Fe_{0.7}O_4$ is 0.251 nm.[33] What's more, the lattice fringe of 0.311 nm near $ZnCo_{1.3}Fe_{0.7}O_4$ (311) crystal plane is attributed to the lattice surface of carbon (002).[34]

The N_2 adsorption–desorption isotherm is exhibited in Fig. 5. The total specific surface area and total pore volume of RHC are 133 $m^2\ g^{-1}$ and 0.16 $cm^3\ g^{-1}$. The total specific surface area of $ZnCo_{1.3}Fe_{0.7}O_4$ is 10 $m^2\ g^{-1}$, and the total pore volume is 0.011 $cm^3\ g^{-1}$. The total specific surface area of $ZnCo_{1.3}Fe_{0.7}O_4$-50%RHC is 37 $m^2\ g^{-1}$, and the total pore volume is 0.08 $cm^3\ g^{-1}$. The specific surface area of $ZnCo_{1.3}Fe_{0.7}O_4$-50%RHC is 3.7 times larger than that of $ZnCo_{1.3}Fe_{0.7}O_4$. It shows that the presence of RHC increases the specific surface area of the prepared nano-material and inhibits the aggregation of nanoparticles. Compared with RHC, the specific surface area of $ZnCo_{1.3}Fe_{0.7}O_4$-50%RHC is reduced because $ZnCo_{1.3}Fe_{0.7}O_4$ nanoparticles occupy the adsorption sites of activated biochar.

The N_2 adsorption–desorption isotherms of $ZnCo_{1.3}Fe_{0.7}O_4$, $ZnCo_{1.3}Fe_{0.7}O_4$-50%RHC and RHC show typical type IV isotherms, confirming that they are mesoporous materials.

It can be seen from the Raman spectrum that RHC and $ZnCo_{1.3}Fe_{0.7}O_4$-50%RHC have two characteristic peaks at near 1349 cm^{-1} and 1585 cm^{-1}. Among them, 1585 cm^{-1} corresponds to the graphite structure (sp^2), and the other peak at 1349 cm^{-1} corresponds to amorphous and polyphase carbon materials.[35] The I_D/I_G of RHC and $ZnCo_{1.3}Fe_{0.7}O_4$-50%RHC are 1.03 and 0.93, respectively. Compared with RHC, the I_D/I_G of $ZnCo_{1.3}Fe_{0.7}O_4$-50%RHC is significantly reduced. That may be because at high temperatures, the catalytic action of Fe and Co causes the unstable carbon atoms to transform from the chaotic layer structure to the graphite crystal structure.

The surface chemical compositions of $ZnCo_{1.3}Fe_{0.7}O_4$-50% RHC complex were determined by XPS. From the wide-scan XPS spectrum of $ZnCo_{1.3}Fe_{0.7}O_4$-50%RHC, the binding energies of 285, 533, 712, 781 and 1023 eV, demonstrate the coexistence of C, O, Fe, Co and Zn in the sample. The C 1s spectrum of $ZnCo_{1.3}Fe_{0.7}O_4$-50%RHC (Fig. 6b) shows three convolution peaks of 284.7, 285.6 and 287.0 eV, corresponding to C–OH

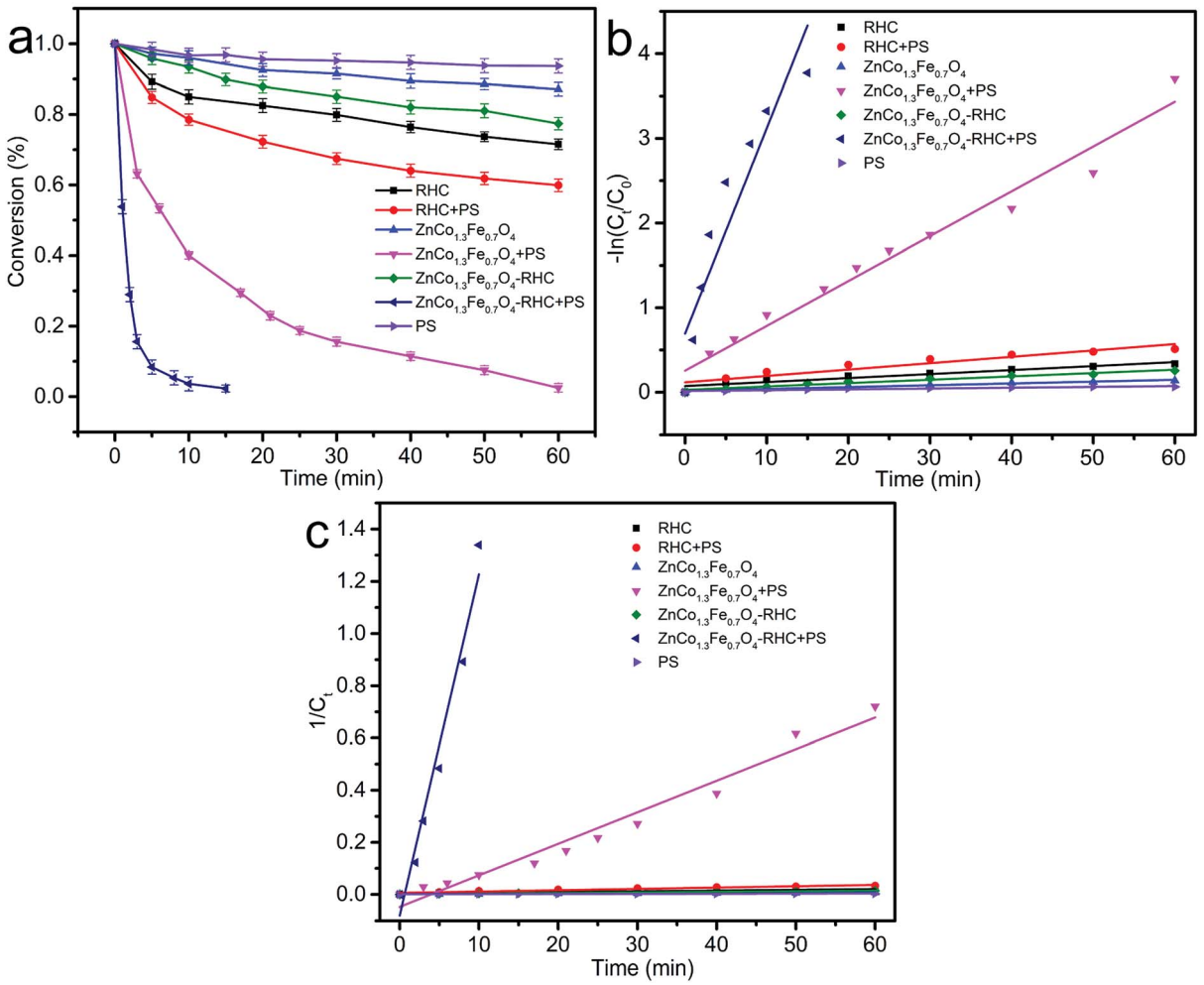

Fig. 7 BPA degradation in different systems (a). Pseudo-first order kinetics model in different systems (b). Pseudo-second order kinetics model in different systems (c). Reaction conditions: [catalyst] = 0.75 g L^{-1}; [PS] = 1.00 g L^{-1}; [BPA] = 20 mg L^{-1}, initial pH = 7, T = 25 °C.

(60.2%), C–O–C (22.2%) and C=O (17.6%).[36] The Fe 2p spectrum is depicted in Fig. 6c. The two main peaks with binding energies of 711.0 eV and 724.5 eV appear on the energy levels of Fe $2p_{3/2}$ and Fe $2p_{1/2}$, which are a typical feature of the ferrite Fe^{3+} respectively.[37] In addition, the Co 2p spectrum (Fig. 6d) at 780.4 and 796.4 eV prove the presence of Co^{3+} in $ZnCo_{1.3}Fe_{0.7}O_4$-50%RHC.[38] In the activation process of PS, Co has higher catalytic activity than Fe. Therefore, it is possible that the substitution of Co^{3+} for Fe^{3+} ions in the spinel $ZnCo_xFe_{2-x}O_4$-50%RHC lattice can improve its catalytic performance.

3.2. Catalytic properties of systems based on $ZnCo_{1.3}Fe_{0.7}O_4$

Fig. 7a shows the effect of RHC, $ZnCo_{1.3}Fe_{0.7}O_4$ and $ZnCo_{1.3}Fe_{0.7}O_4$-RHC on BPA degradation with and without PS. The degradation rate of BPA by PS within 60 min is 6.0% without any catalyst, indicating that it is difficult to degrade BPA when PS exists only. In addition, RHC, $ZnCo_{1.3}Fe_{0.7}O_4$ and $ZnCo_{1.3}Fe_{0.7}O_4$-RHC degrade 28.4%, 12.6% and 22.3% of BPA within 60 min without PS addition, respectively, which is attributed to the adsorption of catalyst on BPA. However, after adding PS to $ZnCo_{1.3}Fe_{0.7}O_4$ and $ZnCo_{1.3}Fe_{0.7}O_4$-RHC, the degradation efficiency of BPA is significantly accelerated and the degradation rate of $ZnCo_{1.3}Fe_{0.7}O_4$-RHC/PS reaches 96.3% within 10 min. It is more effective than RHC/PS (21.2%) and $ZnCo_{1.3}Fe_{0.7}O_4$/PS (58.9%) systems in BPA degradation, showing that $ZnCo_{1.3}Fe_{0.7}O_4$-RHC can activate PS more effectively than RHC and $ZnCo_{1.3}Fe_{0.7}O_4$ for degrading BPA. The adsorption of $ZnCo_{1.3}Fe_{0.7}O_4$-RHC on BPA degradation is not an important factor.

In addition, the $ZnCo_{1.3}Fe_{0.7}O_4$ has synergistic effect with RHC when BPA is degraded by $ZnCo_{1.3}Fe_{0.7}O_4$-RHC system. This is because the degradation efficiency of $ZnCo_{1.3}Fe_{0.7}O_4$-RHC system on BPA (Fig. 7a) is greater than that of RHC/PS and $ZnCo_{1.3}Fe_{0.7}O_4$/PS system on BPA at 10 min, which confirms that RHC plays an important role in improving the catalytic activity of $ZnCo_{1.3}Fe_{0.7}O_4$-RHC composite material. Synergistic effect is shown in: (1) RHC has can prevent the aggregation of part of $ZnCo_{1.3}Fe_{0.7}O_4$ nanoparticles and a large specific surface area during the reaction. (2) RHC and ferrite materials accelerate the electron transfer rate, thus improving the catalytic performance of $ZnCo_{1.3}Fe_{0.7}O_4$ nanoparticles.

The relationship between reaction rate and reaction time of different systems is analyzed by pseudo-first-order and second-order kinetics models. The pseudo-first-order kinetics model (eqn (5)) and second-order kinetics model (eqn (6)) are expressed as follows:[39]

$$\frac{dc}{dt} = -k_1 C \Leftrightarrow \ln(C_t/C_0) = -k_1 t \quad (5)$$

$$\frac{dc}{dt} = -k_2 C^2 \Leftrightarrow \frac{1}{C_t} - \frac{1}{C_0} = k_2 t \quad (6)$$

where C_0 is the initial concentration of BPA, C_t is the concentration of BPA at time t, k_1 is a pseudo-first-order kinetic degradation rate constant, and k_2 is a second-order kinetic degradation rate constant. The experimental data of BPA degradation are fitted, and the results are shown in Table 3. As shown in Fig. 7b and c, the correlation coefficient of the experimental data fitted with the second-order kinetic model ($R_2^2 = 0.9104$–0.9659) is higher than that of the pseudo-first-order kinetic model ($R_1^2 = 0.8550$–0.9617), so the degradation process of BPA should be more in line with the pseudo-second-order kinetic equation. Meanwhile, it can be observed that $ZnCo_{1.3}Fe_{0.7}O_4$-RHC has higher catalytic activity than $ZnCo_{1.3}Fe_{0.7}O_4$ and RHC to degrade BPA in the persulfate system.

3.3. Catalytic properties of Zn,Co,Fe-RHC composites

3.3.1 Effect of the molar ratio of Co to Fe in $ZnCo_xFe_{2-x}O_4$ on the catalytic degradation of BPA. In order to comprehensively evaluate the catalytic performance of $ZnCo_{1.3}Fe_{0.7}O_4$ for BPA degradation, as shown in Fig. 8a, we conducts a series of parallel experiments with ZnO, Fe_3O_4, Fe_2O_3, Co_3O_4 and $ZnCo_{1.3}Fe_{0.7}O_4$ as catalysts. Within 30 minutes, the degradation efficiencies of ZnO, Fe_3O_4, Fe_2O_3, Co_3O_4 and $ZnCo_{1.3}Fe_{0.7}O_4$ to BPA are 19.9%, 29.9%, 35.5%, 56.5% and 82.6%, respectively. Among them, $ZnCo_{1.3}Fe_{0.7}O_4$ has the highest degradation rate of BPA, which shows that the coexistence of Co and Fe improves the catalytic activity of the catalyst. This indicates that in the reaction system, Co and Fe may have a synergistic effect, so that $ZnCo_{1.3}Fe_{0.7}O_4$ has good catalytic activity.

In addition, Fig. 8b shows the effect of Co content on BPA degradation. With the increase of Co content, the catalytic activity of $ZnFe_{2-x}Co_xO_4$ for BPA first increased and then decreased. When $x = 0$, 0.7 and 1.3, the degradation efficiency of $ZnFe_{2-x}Co_xO_4$ to BPA are 67.7%, 87.9% and 97.4% within 60 min, respectively. The results show that a proper proportion of Co doping can promote the activity of $ZnFe_{2-x}Co_xO_4$.

Table 3 Kinetic parameters on BPA degradation of different catalysts

	Pseudo-first-order kinetics		Pseudo-second-order kinetics	
	k_1 (10^{-2} min^{-1})	R_1^2	k_2 (10^{-2} L mg^{-1} min^{-1})	R_2^2
RHC	0.47	0.8786	0.028	0.9127
$ZnCo_{1.3}Fe_{0.7}O_4$	0.22	0.9442	0.012	0.9526
$ZnCo_{1.3}Fe_{0.7}O_4$-RHC	0.40	0.9527	0.023	0.9659
RHC + PS	0.75	0.8594	0.051	0.9104
$ZnCo_{1.3}Fe_{0.7}O_4$ + PS	5.29	0.9617	1.21	0.9651
$ZnCo_{1.3}Fe_{0.7}O_4$-RHC + PS	25.25	0.8550	13.07	0.9599
PS	0.097	0.9126	0.005	0.9497

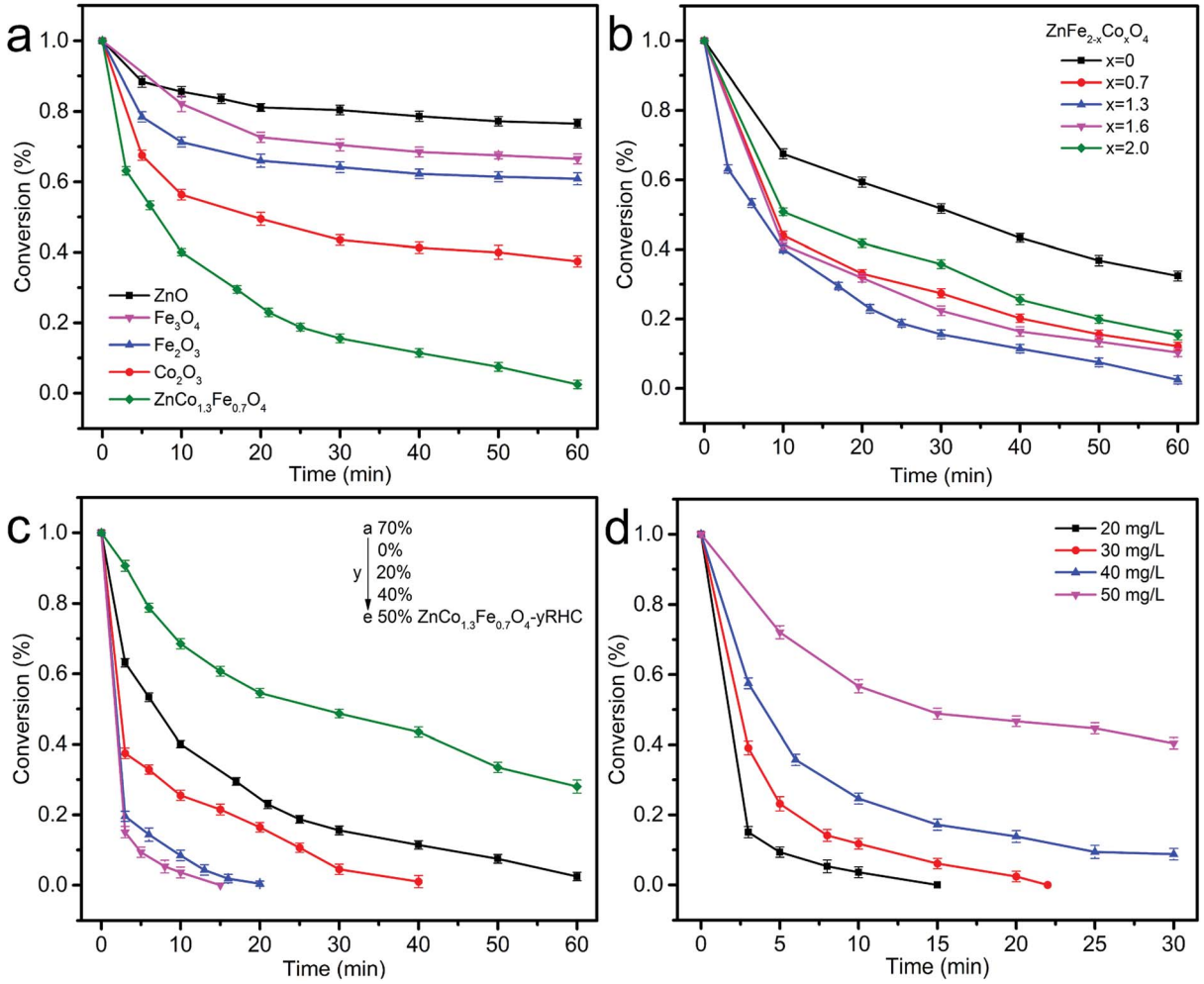

Fig. 8 Degradation of BPA using different catalyst (ZnO, Fe_3O_4, Fe_2O_3, Co_2O_3 and $ZnCo_{1.3}Fe_{0.7}O_4$, respectively) (a). Effect of the molar ratio of Co to Fe in $ZnCo_xFe_{2-x}O_4$ ($x = 0$, 0.7, 1.3, 1.6 and 2, respectively) on the catalytic degradation of BPA using PS as oxidant (b). Effect of RHC content in $ZnCo_{1.3}Fe_{0.7}O_4$-y%RHC ($y = 70$, 0, 20, 40 and 50, from a to e, respectively) on catalytic oxidation of BPA (c). Effect of bisphenol A concentration on catalytic degradation (d). ([catalyst] = 0.75 g L^{-1}, [BPA] = 20 mg L^{-1}, [PS] = 1.00 g L^{-1}, initial pH = 7, T = 25 °C).

However, in the range of 1.3–2, the increase in the molar ratio of Co is inversely proportional to the degradation efficiency. This may be due to the introduction of a large amount of Co in the zinc ferrite to cause the formation of hematite, which has poor catalytic activity for PS.[40,41] Therefore, the Co molar ratio $x = 1.3$ is an appropriate ratio of $ZnFe_{2-x}Co_xO_4$.

3.3.2 Effect of RHC content on the catalytic degradation of BPA. Fig. 8c shows the effect of RHC content on the catalytic degradation of BPA. When RHC content is 0%, 20%, 40% and 50% in $ZnCo_{1.3}Fe_{0.7}O_4$ nanoparticles, the degradation rate of BPA reaches 61.9%, 74.5%, 96.3% and 91.5% within 10 min. It shows that the introduction of RHC increases the surface area of $ZnCo_{1.3}Fe_{0.7}O_4$ nanoparticles, increases the active area between catalyst and reactants during the reaction, and accelerates the reaction process.[42] The unique synergy between ferrite nanoparticles and RHC enhances catalytic activity. However, as the content of RHC increased to 70%, the degradation rate of BPA decreased, and the degradation rate decreased to 31.5% within 10 minutes. This is because the increase of RHC content will inevitably lead to the decrease of $ZnCo_{1.3}Fe_{0.7}O_4$ content, so the catalytic activity of $ZnCo_{1.3}Fe_{0.7}O_4$-y%RHC decreases. Therefore, 50 wt% is selected as the optimal content of RHC.

3.3.3 Effect of bisphenol A concentration on catalytic degradation of BPA. Fig. 8d shows the effect of the initial concentration of BPA on the catalytic performance of $ZnCo_{1.3}Fe_{0.7}O_4$-50%RHC. The concentration of BPA increased from 20 mg L^{-1} to 50 mg L^{-1}, and the degradation rate of BPA decreased from 96.3% to 48.0% within 10 minutes. However, there is a lower concentration of BPA in the industrial waste water. So it is more meaningful to set a lower concentration of BPA from the perspective of practical application.

3.3.4 Effect of the catalyst dosage on the catalytic degradation of BPA. The effect of the $ZnCo_{1.3}Fe_{0.7}O_4$-50%RHC dosages on BPA degradation is shown in Fig. 9a. When the dosage of $ZnCo_{1.3}Fe_{0.7}O_4$-50%RHC is 0.25 g L^{-1}, 0.40 g L^{-1}, 0.50 g L^{-1} and 0.75 g L^{-1}, the catalytic rates of BPA reach 74.1%, 82.6%, 94.85% and 100% within 15 minutes. However, when the dosage of $ZnCo_{1.3}Fe_{0.7}O_4$-50%RHC is increased to 1.00 g L^{-1}, $ZnCo_{1.3}Fe_{0.7}O_4$-50%RHC has an inhibitory effect on the

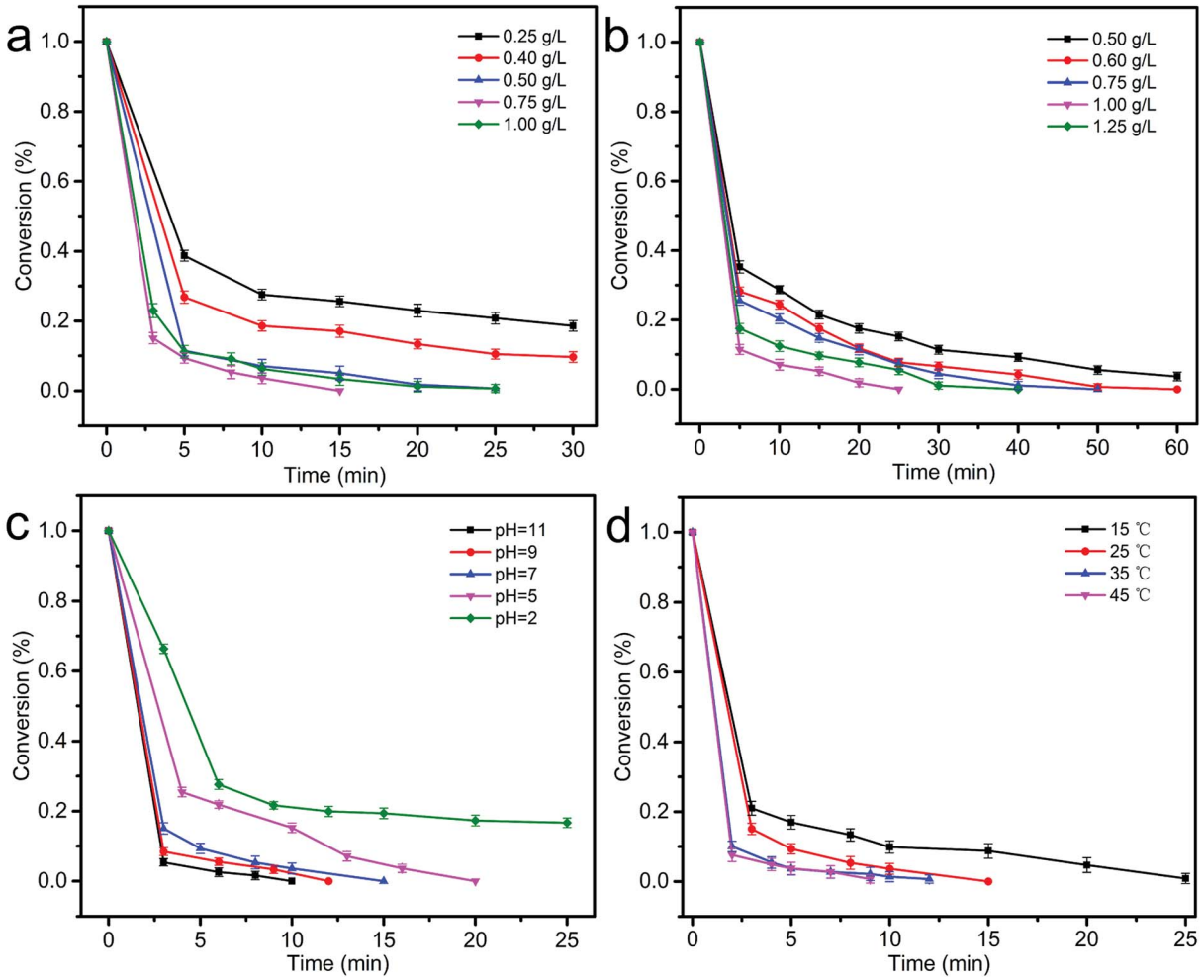

Fig. 9 Effect of the catalyst dosage on the catalytic degradation of BPA (a). Effect of the PS dosage on the catalytic degradation of BPA (b), effect of pH on the catalytic performance of $ZnCo_{1.3}Fe_{0.7}O_4$-50%RHC (c). Effect of temperature on the catalytic performance of $ZnCo_{1.3}Fe_{0.7}O_4$-50% RHC (d). ([catalyst] = 0.75 g L^{-1}, [BPA] = 20 mg L^{-1}, [PS] = 1.00 g L^{-1}, initial pH = 7, T = 25 °C).

degradation of BPA, which is due to excessive catalytic active sites (Fe^{2+}, Co^{2+}) quenching effect on $SO_4^{\bullet-}$ (eqn (7) and (8)).[43]

$$Co^{2+} + SO_4^{\bullet-} \rightarrow SO_4^{2-} + Co^{3+} \quad (7)$$

$$Fe^{2+} + SO_4^{\bullet-} \rightarrow SO_4^{2-} + Fe^{3+} \quad (8)$$

3.3.5 Effect of the PS dosage on the catalytic degradation of BPA. The effect of PS concentration on BPA degradation in $ZnCo_{1.3}Fe_{0.7}O_4$-50%RHC/PS system is studied, and as shown in Fig. 9b. When the concentration of PS increased from 0.5 g L^{-1} to 1.00 g L^{-1}, the BPA degradation rate of $ZnCo_{1.3}Fe_{0.7}O_4$-50% RHC/PS system increased from 78.6% to 94.9% within 15 min. However, when the concentration of PS further increased to 1.25 g L^{-1}, the degradation rate of BPA decreased to 90.0% within 15 min. It suggests that higher PS concentration does not lead to better BPA degradation rates. This may be caused by the auto-coupling reaction of $SO_4^{\bullet-}$ (eqn (9) and (10)).[44,45]

$$SO_4^{\bullet-} + SO_4^{\bullet-} \rightarrow S_2O_8^{2-} \quad (9)$$

$$SO_4^{\bullet-} + S_2O_8^{2-} \rightarrow S_2O_8^{\bullet-} + SO_4^{2-} \quad (10)$$

3.3.6 Effect of pH on the catalytic performance of $ZnCo_{1.3}Fe_{0.7}O_4$-50%RHC. Solution pH has a significant impact on the performance of various redox systems. Fig. 9c shows the effect of solution pH on the catalytic oxidation of BPA. As the pH value increases, the degradation rate of BPA also increases, indicating that the $ZnCo_{1.3}Fe_{0.7}O_4$-50%RHC composite can increase the degradation rate of BPA under alkaline conditions. Because Co^{2+} on the surface of $ZnCo_{1.3}Fe_{0.7}O_4$-50%RHC reacts with H_2O to form $CoOH^+$ (eqn (11)). $CoOH^+$ activates PS to generate $SO_4^{\bullet-}$ (eqn (12)).[46] $SO_4^{\bullet-}$ has a high redox potential and can efficiently oxidize BPA. Under alkaline conditions, $SO_4^{\bullet-}$ can be transformed into surface-bound hydroxyl radicals ($^{\bullet}OH$) (eqn (13)).[47] Under acidic conditions, the production of $CoOH^+$ is limited.[48] In addition, under acidic conditions, excess hydrogen ions can scavenge sulfate radicals and hydroxyl radicals to adversely affect catalysis (eqn (14)). And strong acid conditions inhibit the activation of persulfate through acid

catalyzing persulfate (eqn (15) and (16)).[49] Therefore, alkaline conditions are conducive to the degradation of BPA.

$$Co^{2+} + H_2O \rightarrow CoOH^+ \quad (11)$$

$$CoOH^+ + S_2O_8^{2-} \rightarrow CoOH^{2+} + SO_4^{2-} + SO_4^{\cdot -} \quad (12)$$

$$SO_4^{\cdot -} + OH^- + H^+ \rightarrow {}^{\cdot}OH + SO_4^{2-} + H^+ \quad (13)$$

$$SO_4^{\cdot -}/{}^{\cdot}OH + H^+ + e^- \rightarrow HSO_4^{\cdot -}/H_2O \quad (14)$$

$$H^+ + S_2O_8^{2-} \rightarrow HS_2O_8^- \quad (15)$$

$$HS_2O8- + H_2O \rightarrow H_2SO_5 + HSO_4^- \quad (16)$$

3.3.7 Effect of temperature on the catalytic performance of $ZnCo_{1.3}Fe_{0.7}O_4$-50%RHC. The effect of temperature on BPA degradation is shown in Fig. 9d. It can be seen from that the degradation rate is positively correlated with the reaction temperature. When the temperature drops from 25 °C to 15 °C, the time for complete BPA degradation increase from 15 min to 25 min. When the temperature increases to 35 °C and 45 °C, the complete BPA degradation reaction time are 12 min and 9 min. With the temperature from 15 °C to 45 °C, k of BPA degradation increases greatly from 0.0896 to 0.3448 min^{-1}. It has been reported[50] that high temperature could promote PS decomposition to form active radicals and also speed up the collision frequency between PS and pollutants and catalysts. According to Arrhenius equation $\ln k = \frac{-E_a}{RT} + \ln A$, where k is the rate constant, universal gas constant $R = 8.314$ J mol^{-1} K^{-1}, and A is a constant. The E_a of the $ZnCo_{1.3}Fe_{0.7}O_4$-50%RHC activated PS system is 34.24 kJ mol^{-1}, which is lower than previously reported E_a of BPA degradation activated only by heating (133.5 kJ mol^{-1}).[51] However, due to the high requirements for high temperature energy input, high temperature is not suitable for large-scale applications for considering actual production. In addition, the catalytic performance of $ZnCo_{1.3}Fe_{0.7}O_4$-50% RHC is compared with the recently reported catalysts (Table 4), and the catalytic performance of $ZnCo_{1.3}Fe_{0.7}O_4$-50%RHC is significantly better than that of other catalysts.

3.4. Effect of anions

In general, inorganic salts are abundant in water bodies. The effects of Cl^-, NO_3^-, HCO_3^- and $H_2PO_4^-$ 4 inorganic anions on BPA degradation in $ZnCo_{1.3}Fe_{0.7}O_4$-RHC/PS system are explored.

3.4.1 Effect of Cl^- on the catalytic performance of $ZnCo_{1.3}Fe_{0.7}O_4$-50%RHC. Fig. 10a shows the effect of Cl^- concentration on catalytic degradation of BPA. When the Cl^- concentration increases from 0 mM to 10 mM, the degradation rate of BPA decreases with the increase of Cl^- concentration. However, when the Cl^- concentration increases from 10 mM to 30 mM, the degradation rate of BPA increases with the increase of Cl^- concentration. This may be under the condition of low Cl^- concentration, both $SO_4^{\cdot -}$ or ${}^{\cdot}OH$ are likely to oxidize Cl^- to the less reactive $Cl^{\cdot}$ and $HOCl^-$ ($E^0(Cl_2/Cl^-) = 1.36$ V, E^0(HOCl/Cl^-) = 1.36 V) (eqn (17)–(19)).[55] At a high Cl^- concentration, excessive Cl^- in $ZnCo_{1.3}Fe_{0.7}O_4$-RHC/PS system will react with PS to form highly oxidizing HOCl and Cl_2 (eqn (20) and (21)).[56] Therefore, Cl^- can increase the degradation rate of BPA in a certain range.

$$Cl^- + {}^{\cdot}OH \rightarrow HOCl^{\cdot -} \quad (17)$$

$$HOCl^{\cdot -} + H^+ \rightarrow Cl^{\cdot} + H_2O \quad (18)$$

$$Cl^- + SO_4^{\cdot -} \rightarrow Cl^{\cdot} + SO_4^{2-} \quad (19)$$

$$Cl^- + HSO_5^- \rightarrow SO_4^{2-} + HOCl \quad (20)$$

$$2Cl^- + HSO_5^- + H^+ \rightarrow SO_4^{2-} + Cl_2 + H_2O \quad (21)$$

3.4.2 Effect of NO_3^- on the catalytic performance of $ZnCo_{1.3}Fe_{0.7}O_4$-50%RHC. Fig. 10b shows the effect of NO_3^- concentration on catalytic BPA degradation. It can be seen that NO_3^- has almost no effect on the degradation of BPA in $ZnCo_{1.3}Fe_{0.7}O_4$-RHC/PS system, and the degradation curves of BPA by different concentrations of NO_3^- are almost identical. This is due to the reaction rate of NO_3^- and $SO_4^{\cdot -}$ is slow ($k = (5.6 \pm 0.5) \times 10^4$ M^{-1} s^{-1}) and the weak reactivity of $NO_3^{\cdot}$ (eqn (22)).[57] In addition, NO_3^- does not generate other free radicals with PS. Moreover, $ZnCo_{1.3}Fe_{0.7}O_4$-RHC/PS system has good stability and is not easily affected by changes of external environment.

$$SO_4^{\cdot -} + NO_3^- \rightarrow SO_4^{2-} + NO_3^{\cdot} \quad (22)$$

3.4.3 Effect of HCO_3^- on the catalytic performance of $ZnCo_{1.3}Fe_{0.7}O_4$-50%RHC. As shown in Fig. 10c, the influence of different concentrations of HCO_3^- on the catalytic oxidation of BPA by $ZnCo_{1.3}Fe_{0.7}O_4$-RHC is investigated. As can be seen from the figure, with the concentration of HCO_3^- increasing from 0 mM to 30 mM, the BPA degradation rate decreases from

Table 4 Comparison of catalytic performance of $ZnCo_{1.3}Fe_{0.7}O_4$-50%RHC with recently reported catalysts toward the degradation of BPA[a]

Catalyst	m_{cat} (g L^{-1})	m_{PS} (mg L^{-1})	C_{BPA} (mg L^{-1})	Time (min)	R (%)	Ref.
$ZnCo_{1.3}Fe_{0.7}O_4$-50%RHC	0.75	1.00	20	15	100	This work
Fe_3S_4	0.2	0.22	5	120	95	52
$CuFe_2O_4$/kaolinite	0.5	0.5	50	60	100	53
$Mn_{0.6}Zn_{0.4}Fe_2O_4$	0.2	0.5	10	60	100	54

[a] m_{cat} is the dosage of catalyst, m_{PS} is the dosage of PS, C_{BPA} is the concentration of BPA, R is the removal efficiency.

96.3% to 59.6% within 10 min. Because HCO_3^- and CO_3^{2-} react with strongly oxidizing $SO_4^{\cdot-}$ to produce less oxidizing $CO_3^{\cdot-}$ and $HCO_3^{\cdot}$ (eqn (23)–(27)), so HCO_3^- inhibits BPA degradation.[58]

$$SO_4^{\cdot-} + HCO_3^- \rightarrow SO_4^{2-} + HCO_3^{\cdot} \quad (23)$$

$$\cdot OH + HCO_3^- \rightarrow H_2O + HCO_3^{\cdot} \quad (24)$$

$$CO_3^{2-} + SO_4^{\cdot-} \rightarrow SO_4^{2-} + CO_3^{\cdot-} \quad (25)$$

$$^{\cdot}OH + HCO_3^- \rightarrow CO_3^{2-} + H_2O \quad (26)$$

$$CO_3^{2-} + {}^{\cdot}OH \rightarrow OH^- + CO_3^{\cdot-} \quad (27)$$

3.4.4 Effect of $H_2PO_4^-$ on the catalytic performance of $ZnCo_{1.3}Fe_{0.7}O_4$-50%RHC. As shown in Fig. 10d, the effect of different concentrations of $H_2PO_4^-$ on the catalytic oxidation of BPA by $ZnCo_{1.3}Fe_{0.7}O_4$-RHC is investigated. Fig. 10d shows that the degradation rate of BPA decreases with the increase of $H_2PO_4^-$ concentration, indicating that the presence of $H_2PO_4^-$ inhibits the degradation of BPA. The effect of $H_2PO_4^-$ on catalytic oxidation of BPA by $ZnCo_{1.3}Fe_{0.7}O_4$-RHC was far greater than that of Cl^-, NO_3^- and HCO_3^-. This is due to the affinity of $H_2PO_4^-$ to $ZnCo_{1.3}Fe_{0.7}O_4$-RHC, and binds to the Co–OH on the surface of $ZnCo_{1.3}Fe_{0.7}O_4$ through a chelation reaction, reducing the catalytic activity of Co (eqn (28)–(30)). Therefore, the inhibition of $H_2PO_4^-$ on the degradation of BPA by $ZnCo_{1.3}Fe_{0.7}O_4$-RHC can be considered to be related to the substitution of hydroxyl groups on the catalyst surface.[59]

$$Co\text{–}OH + H_2PO_4^- \leftrightarrow CoH_2PO_4 + OH^- \quad (28)$$

$$Co\text{–}OH + H_2PO_4^- \leftrightarrow CoHPO_4^- + H_2O \quad (29)$$

$$Co\text{–}OH + H_2PO_4^- \rightarrow CoPO_4^{2-} + H_2O + H^+ \quad (30)$$

3.5. Stability and reusability

The stability and cyclability of $ZnCo_{1.3}Fe_{0.7}O_4$-RHC are very important to its practical application. In order to determine the cyclability and stability of $ZnCo_{1.3}Fe_{0.7}O_4$-RHC in PS oxidation system, the particles are recovered (such as centrifugation and

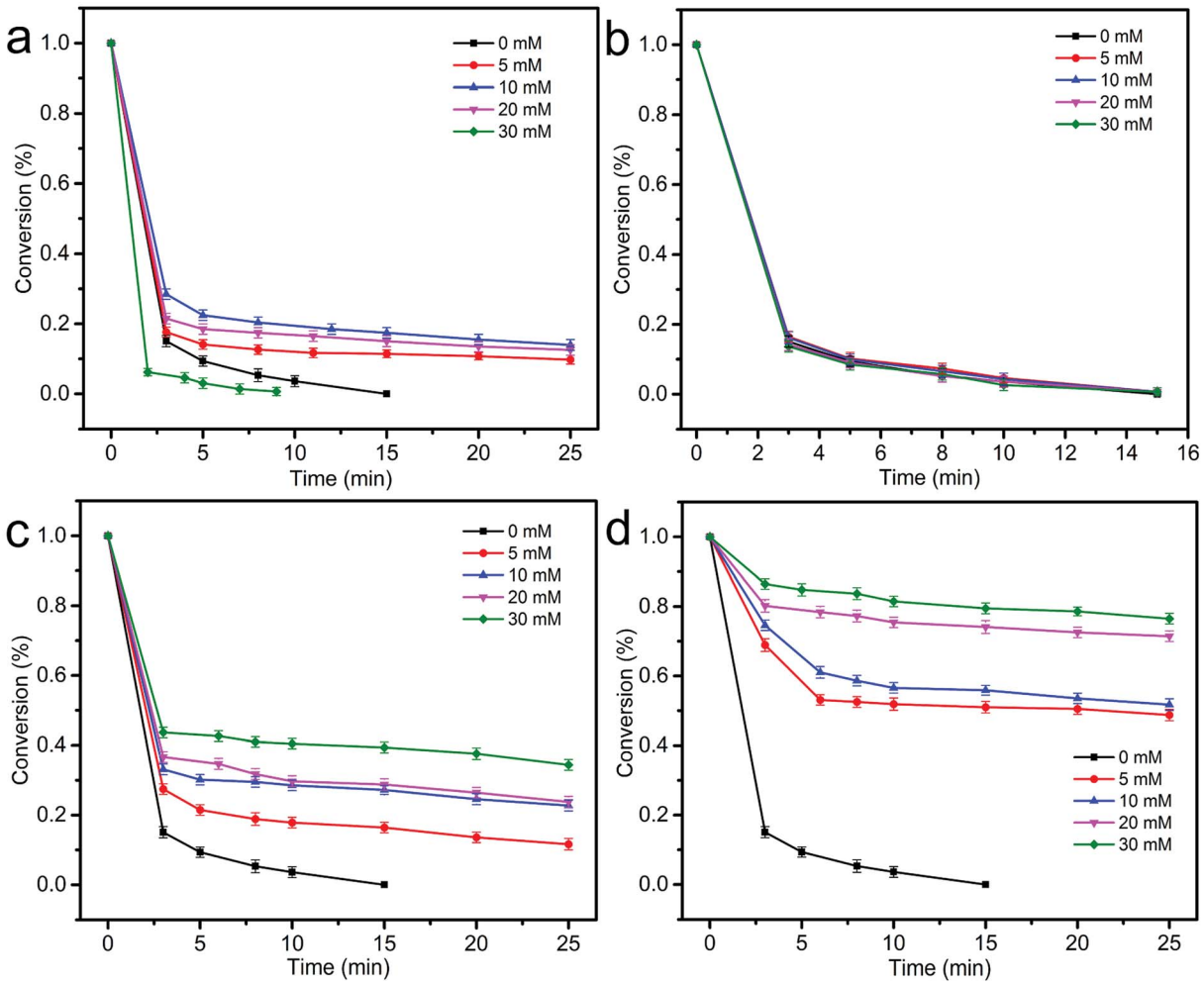

Fig. 10 Effect of various co-anion on BPA degradation: Cl^- (a), NO_3^- (b), HCO_3^- (c), $H_2PO_4^-$ (d). ([catalyst] = 0.75 g L^{-1}, [BPA] = 20 mg L^{-1}, [PS] = 1.00 g L^{-1}, initial pH = 7, T = 25 °C).

magnetic adsorption), washed multiple times with deionized water and ethanol, and dried at 70 °C. $ZnCo_{1.3}Fe_{0.7}O_4$-RHC still maintained good catalytic activity, and BPA can be completely degraded within 40 min after 5 consecutive uses (Fig. 11a). The catalytic activity of $ZnCo_{1.3}Fe_{0.7}O_4$-RHC does not decrease significantly. The slight decrease in BPA degradation rate after 5 cycles is due to the slight aggregation of $ZnCo_{1.3}Fe_{0.7}O_4$-RHC, resulting in the reduction of catalytic active sites. As shown in the inset of Fig. 11a, the homogeneously dispersed $ZnCo_{1.3}Fe_{0.7}O_4$-50%RHC is collected by simply applying a magnetic field. The result strongly indicates that $ZnCo_{1.3}Fe_{0.7}O_4$-50%RHC has considerable magnetic. In addition, comparing the XRD and FTIR patterns of $ZnCo_{1.3}Fe_{0.7}O_4$-RHC before and after the reaction (Fig. 11b and c), no significant changes are found, indicating that $ZnCo_{1.3}Fe_{0.7}O_4$-RHC composite maintains good reuse performance and long service life. Meanwhile, the leaching concentration of metal ions in $ZnCo_{1.3}Fe_{0.7}O_4$-RHC after each cycle was measured by ICP (Fig. 11d). The leaching concentrations of Zn, Fe and Co are all less than 53.3 μg L^{-1}, 31.2 μg L^{-1} and 48.7 μg L^{-1}, which are lower than Chinese industrial wastewater discharge standards (GB 8978-2002).[60] Compared with cobalt ferrite with no Zn added (Table 5), the leaching rate of each element decreased. This may be due to the smaller ion radius of Zn^{2+}, the electrostatic coulomb force increases, so that Zn and Co attract more closely.[26] After the reaction, the metal content of $ZnCo_{1.3}Fe_{0.7}O_4$-RHC composite material did not change much, indicating that $ZnCo_{1.3}Fe_{0.7}O_4$-RHC composite material has good stability.

3.6. Radical identification and catalytic mechanism

The early report has confirmed that PS could be activated to generate free radicals to oxidize organic pollutants, that is, degradation through free radical pathway.[64] Therefore, the degradation efficiency of organic pollutants was inhibited after adding free radical capture agent. However, Duan *et al.*[65] used

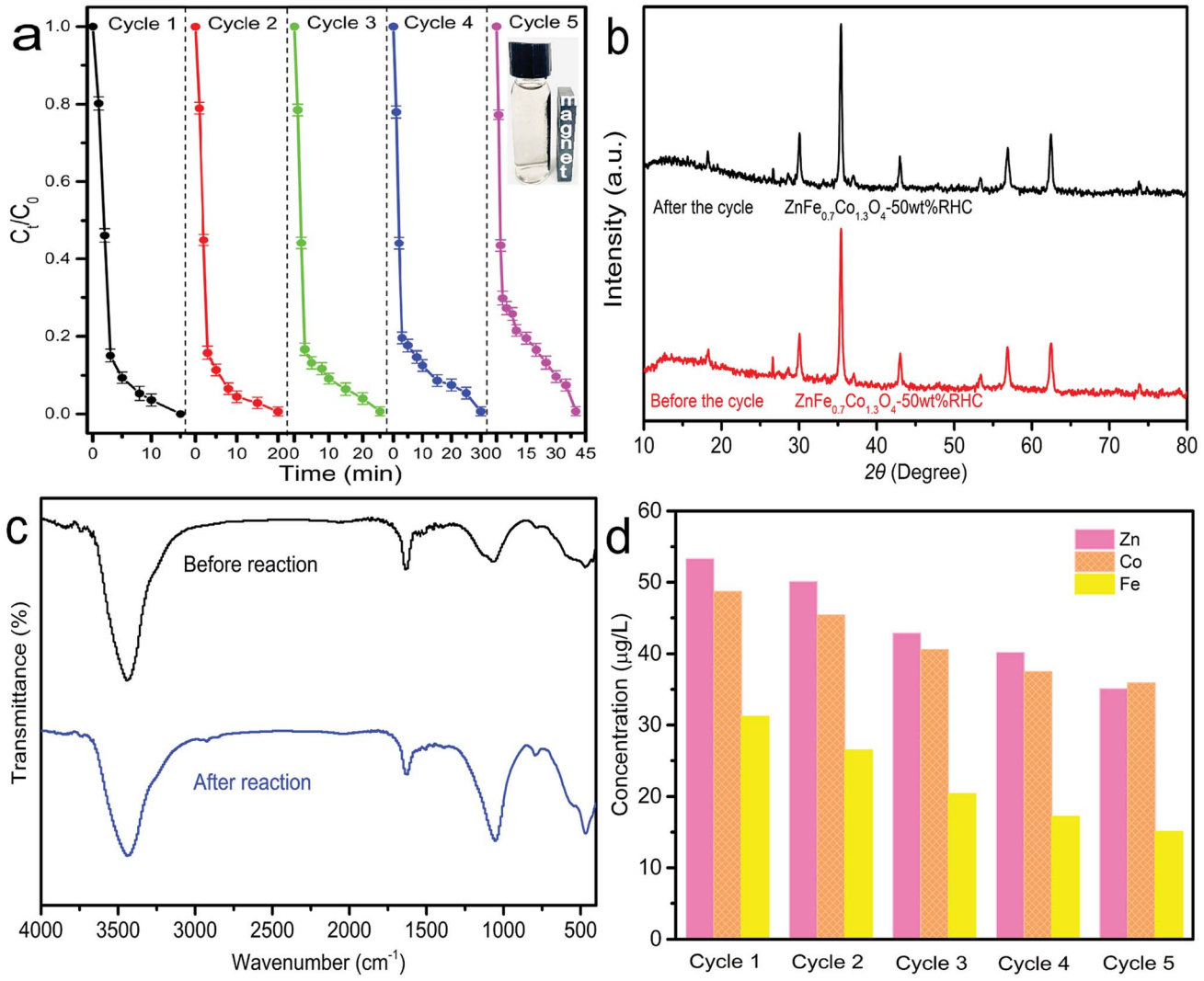

Fig. 11 The reusability of $ZnCo_{1.3}Fe_{0.7}O_4$-RHC for BPA degradation in presence of PMS (a). XRD patterns of $ZnCo_{1.3}Fe_{0.7}O_4$-RHC before and after the reaction (b). FTIR patterns of $ZnCo_{1.3}Fe_{0.7}O_4$-RHC before and after the reaction (c). The leakage of Fe, Co and Zn ions after five cycles of BPA degradation by $ZnCo_{1.3}Fe_{0.7}O_4$-RHC and PMS system (d). ([catalyst] = 0.75 g L^{-1}, [BPA] = 20 mg L^{-1}, [PS] = 1.00 g L^{-1}, initial pH = 7, T = 25 °C).

Table 5 Comparison of leaching rate of each element of $ZnCo_{1.3}Fe_{0.7}O_4$-50%RHC with recently reported $CoFe_2O_4$ catalysts after degradation of BPA

Catalyst	Co ($\mu g\ L^{-1}$)	Fe ($\mu g\ L^{-1}$)	Ref.
$ZnCo_{1.3}Fe_{0.7}O_4$-50%RHC	48.7	31.2	This work
$CoFe_2O_4$	410	50	61
$CoFe_2O_4$@graphene	430	160	60
$CoFe_2O_4$-SAC	570	250	62
$CoFe_2O_4$	763	68	63

nitrogen-doped carbon nanotubes to degrade phenol through a non-radical process. The degradation rate of organic pollutants is not completely inhibited by the addition of high concentration of free radical trapping agents. Therefore, it is necessary to determine main active substances and reaction pathway in $ZnCo_{1.3}Fe_{0.7}O_4$-RHC/PS system.

The main active substances are determined by the corresponding free radical capture experiment in $ZnCo_{1.3}Fe_{0.7}O_4$-RHC/PS system.[66] Adding EtOH and TBA to the reaction system can distinguish the contribution of $SO_4^{\bullet-}$ and $^{\bullet}OH$ to the $ZnCo_{1.3}Fe_{0.7}O_4$-RHC/PS system. Because EtOH can quickly react with $SO_4^{\bullet-}$ ($k = 1.6 \times 10^7\ M^{-1}\ s^{-1}$) and $^{\bullet}OH$ ($1.9 \times 10^9\ M^{-1}\ s^{-1}$). Besides, TBA can react quickly with $^{\bullet}OH$ ($k = 6.0 \times 10^7\ M^{-1}\ s^{-1}$), and react slowly with $SO_4^{\bullet-}$ ($k = 4.0 \times 10^5\ M^{-1}\ s^{-1}$).[63] As shown in Fig. 12a, with the increase of TBA concentration, the degradation rate of BPA decreases from 100% to 26.8% within 15 minutes (n[TBA/PS] = 1000). TBA inhibited the degradation of BPA, confirming the existence of $^{\bullet}OH$ in the system. Compared with TBA, EtOH further inhibits the degradation of BPA, and the degradation rate of BPA is reduced from 100% to 9.1% within 15 minutes (n[EtOH/PS] = 1000, Fig. 12b). It shows that besides $^{\bullet}OH$, there is also $SO_4^{\bullet-}$ in $ZnCo_{1.3}Fe_{0.7}O_4$-RHC/PS system. BQ and FFA are used as capture agents for $O_2^{\bullet-}$ ($k = 9.6 \times 10^8\ M^{-1}\ s^{-1}$) and $^1O_2$ ($k = 2 \times 10^9\ M^{-1}\ s^{-1}$).[67] Fig. 12c shows that in the presence of BQ, the degradation efficiency of BPA can still reach 100%. The result shows that $O_2^{\bullet-}$ does not participate in the oxidative degradation of BPA. However, the degradation rate of BPA is reduced, because BQ is adsorbed on the surface of the catalyst through the interaction with RHC, which hinders the activation of PS by the catalyst. After adding FFA, the degradation rate of BPA within 50 minutes is only 51.3% (n[FFA/PS] = 600). It shows that $^1O_2$ plays an important role in the degradation of BPA in the $ZnCo_{1.3}Fe_{0.7}O_4$-RHC/PS system.

The types of free radicals produced during the reaction are further determined by ESR. Fig. 12d shows that $ZnCo_{1.3}Fe_{0.7}O_4$-RHC activates PS with 7 typical DMPO-X peaks, and shows strong $^{\bullet}OH$ and $SO_4^{\bullet-}$ radical signals, indicating the presence of $^{\bullet}OH$ and $SO_4^{\bullet-}$ in the reaction system of $ZnCo_{1.3}Fe_{0.7}O_4$-RHC. The signal of $SO_4^{\bullet-}$ is stronger than that of $^{\bullet}OH$. Since $^{\bullet}OH$ is produced by the reaction of $SO_4^{\bullet-}$ with H_2O (eqn (32)), and $SO_4^{\bullet-}$ determines the amount of $^{\bullet}OH$. It further illustrates that $SO_4^{\bullet-}$ plays a dominant role in degradation. Fig. 12e shows the ESR test results using TEMP as the capture agent. It shows a typical ternary peak with an intensity of 1 : 1 : 1, confirming the presence of $^1O_2$. Based on the results of free radical capture experiment and ESR test, $SO_4^{\bullet-}$ dominates the $ZnCo_{1.3}Fe_{0.7}O_4$-RHC/PS degradation system, and $^{\bullet}OH$ and $^1O_2$ play important roles.

Even when EtOH, TBA, and FFA are added to the $ZnCo_{1.3}Fe_{0.7}O_4$-RHC/PS degradation system at the molar ratio of EtOH/PS = 1000, TBA/PS = 1000, and FFA/PS = 6000, BPA can not be completely degraded. This indicates that there may be a non-radical process in the $ZnCo_{1.3}Fe_{0.7}O_4$-RHC/PS system.[65]

In this study, the synergy between $ZnCo_{1.3}Fe_{0.7}O_4$ nanoparticles and RHC also plays a crucial role in the excellent catalytic performance of $ZnCo_{1.3}Fe_{0.7}O_4$-RHC/PS. Studies[68] have been reported that catalyst with graphitized structure could induce non-radical process, by using the carbon-based graphitized structure as a bridge to transfer electrons between the target pollutant and PS. And in this study, the electrons in Co(II) and Fe(II) can be easily transferred to the sp^2 hybridized carbon in the graphitized structure, so that RHC has a large number of free-flowing delocalized π electrons. RHC with a large number of free-flowing delocalized electrons promotes the transfer of electrons from BPA (electron donor) adsorbed on the surface of $ZnCo_{1.3}Fe_{0.7}O_4$-RHC to PS to generate reactive complexes (electron acceptors). Furthermore, Fig. 8c also shows that when the RHC content increases from 0% to 50%, the degradation rate of BPA increases by 36.4% within 15 minutes, indicating that part of BPA degradation is realized through the non-free radical pathway of RHC.

By comparing the XPS spectra of $ZnCo_{1.3}Fe_{0.7}O_4$-RHC before and after the reaction, the activation mechanism of PS and transition metals in $ZnCo_{1.3}Fe_{0.7}O_4$-RHC system is investigated (Fig. 13). The change of Co $2p_{3/2}$ in $ZnCo_{1.3}Fe_{0.7}O_4$-RHC after reaction is observed in Fig. 13c, showing that 44.4% of Co(III) is converted to Co(II). Moreover, compared with the binding energy of 780.4 eV of Co before catalytic reaction, the binding energy of Co after reaction is converted to a higher 780.9 eV. $S_2O_8^{2-}$ reacts with H_2O to produce HSO_5^- (eqn (31)). Since the redox potential of Co(III)/Co(II) (1.81 V) is higher than that of $HSO_5^-/SO_5^{\bullet-}$ (1.10 V), $HSO_5^-/SO_5^{\bullet-}$ can reduce Co(III) to Co(II) (eqn (32)).[69] Then, Co(II) is oxidized by $S_2O_8^{2-}$ to produce Co(III), which realizes the cyclic regeneration of Co(III) and Co(II) (eqn (33)). Fe 2p also shows similar changes to Co 2p. In the used $ZnCo_{1.3}Fe_{0.7}O_4$-RHC catalyst, Fe(III) accounts for 52.8% and Fe(II) accounts for 47.2%. H_2O can be dissociated on Fe^{3+} to form $FeOH^{2+}$ (eqn (34)). $FeOH^{2+}$ can easily interact with Co(II) to form $CoOH^+$ (eqn (35)). Besides, the highly reactive Co(II) reacts with H_2O to form $CoOH^+$ (eqn (36)). $CoOH^+$ reacts directly with $S_2O_8^{2-}$ to generate $SO_4^{\bullet-}$ (eqn (9)). $SO_4^{\bullet-}$ can react with H_2O to generate $^{\bullet}OH$ (eqn (11)). At the same time, Fe(III) is reduced by $S_2O_8^{2-}$ to produce Fe(II) (eqn (37)). However, the redox potential of Fe(III)/Fe(II) (0.77 V) is lower than that of $HSO_5^-/SO_5^{\bullet-}$ (1.10 V), so Fe(III) cannot be reduced by HSO_5^-. Then, Fe(II) is oxidized by $SO_4^{\bullet-}$ or $^{\bullet}OH$ to produce Fe(III) (eqn (38)), achieving Fe(III) regeneration. These results indicate that both redox pairs Co(III)/Co(II) and Fe(III)/Fe(II) are involved in the activation of PS by $ZnCo_{1.3}Fe_{0.7}O_4$-RHC. In addition, FFA free radical capture experiment and TEMP capture experiment have confirmed that $^1O_2$ plays an important role in BPA degradation process.

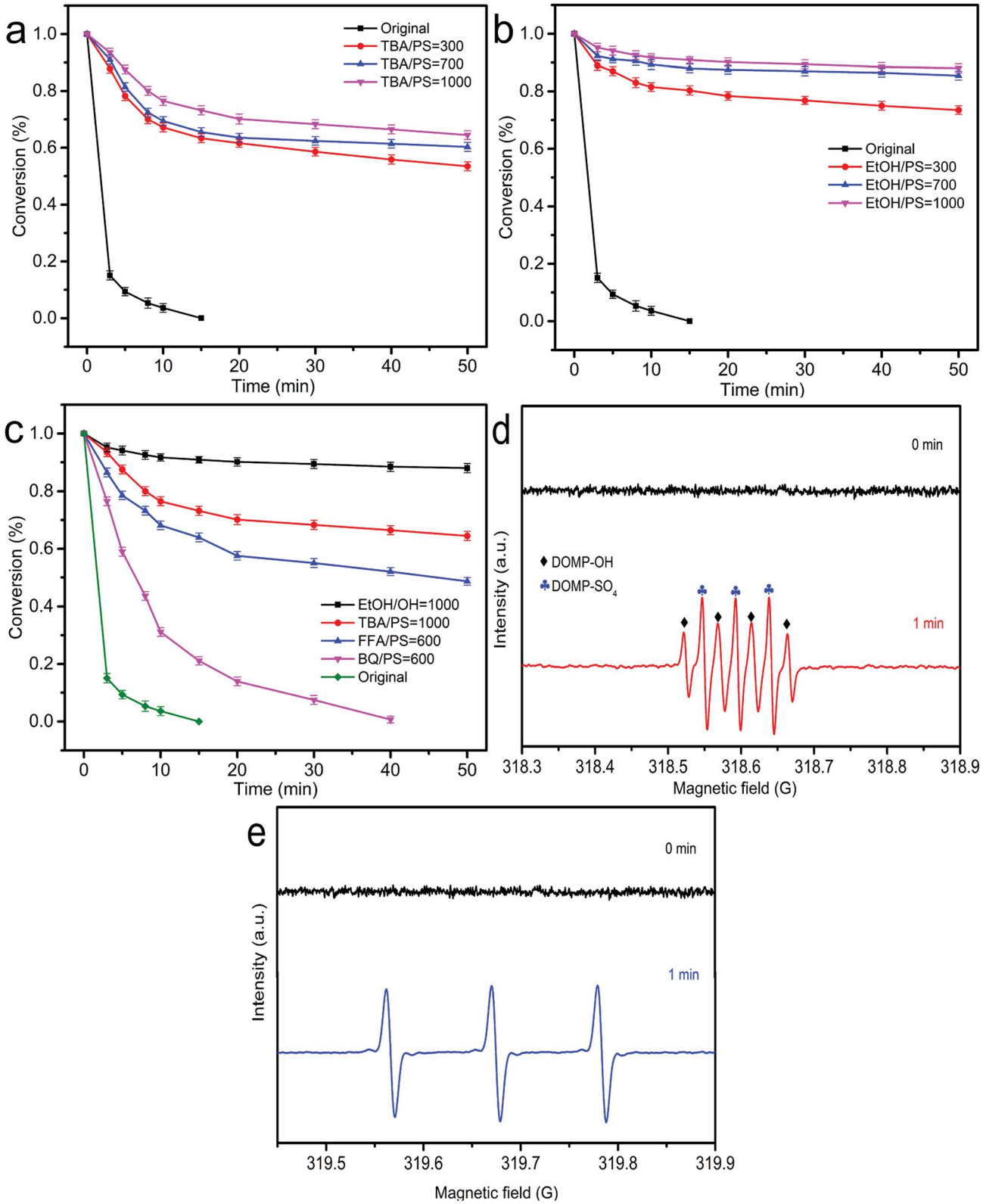

Fig. 12 Effect of TBA (a), EtOH (b) (with different molar ratio to PS) on the degradation of BPA. Effect of BQ and FFA (with fixed molar ratio to PS) on the degradation of BPA (c). ESR tests of $SO_4^{\bullet-}$, $^{\bullet}OH$ (d) and $^1O_2$ (e). ([catalyst] = 0.75 g L^{-1}, [BPA] = 20 mg L^{-1}, [PS] = 1.00 g L^{-1}, initial pH = 7, T = 25 °C).

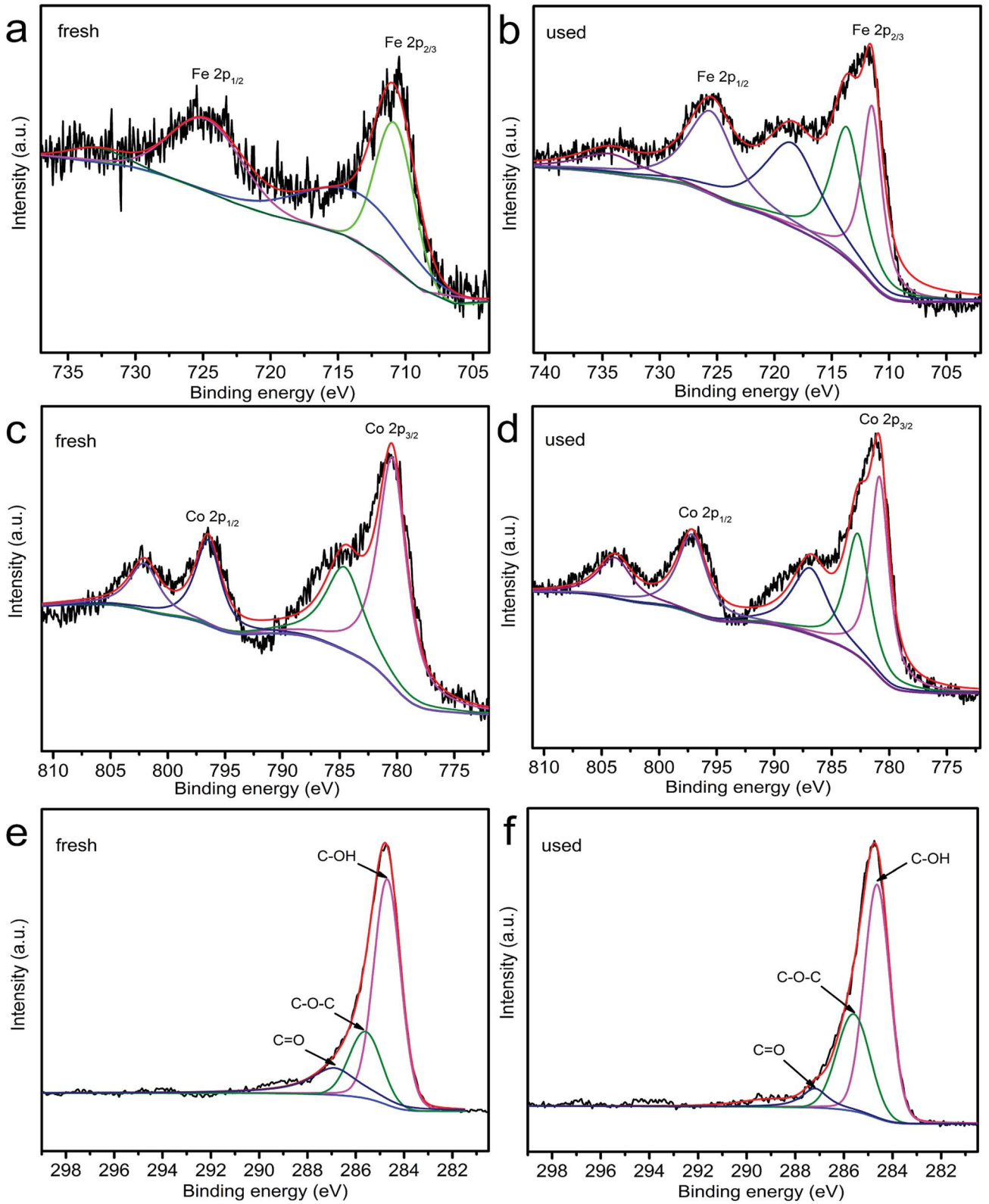

Fig. 13 XPS spectra of Fe 2p, Co 2p and C for fresh (a, c, e) and used (b, d, f) $ZnCo_{1.3}Fe_{0.7}O_4$-RHC.

Compared with the C XPS spectra of unused and used $ZnCo_{1.3}Fe_{0.7}O_4$-RHC, the content of C=O functional group decreases from 17.6% to 6.2%, while the content of C–O–C functional group increases from 22.2% to 32.8%, and the content of C–OH functional group increases from 60.2% to 61.0%. It has been reported that C=O could promote the self-decomposition of PS, thereby producing produce $^1O_2$.[70] The C XPS spectrum further confirms the importance of $^1O_2$ in the

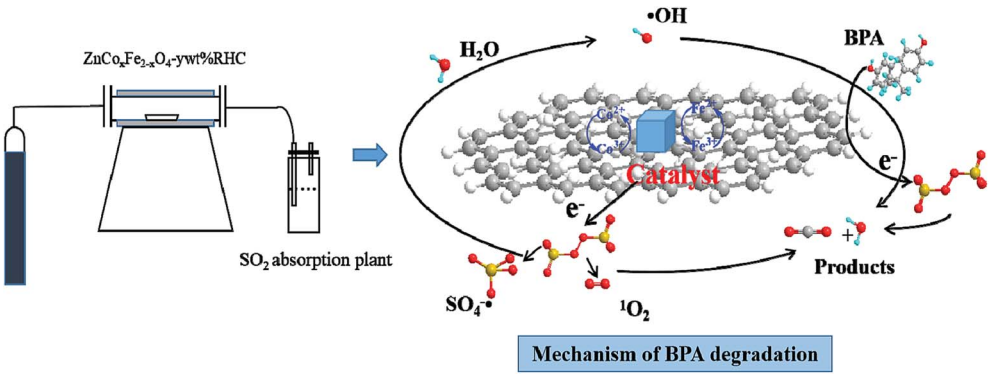

Fig. 14 Mechanism of the activation on PS by $ZnCo_{1.3}Fe_{0.7}O_4$-RHC for the degradation of BPA.

degradation system of $ZnCo_{1.3}Fe_{0.7}O_4$-RHC/PS. The HSO_5^- is produced in the reaction self-decomposes to produce SO_5^{2-} (eqn (39)). What's more, $SO_5^{\cdot-}$ interacts with HSO_5^- to generate $^1O_2$ (eqn (40)). And $SO_5^{\cdot-}$ can react with itself or H_2O to generate $^1O_2$ (eqn (41)–(43)). Finally, $ZnCo_{1.3}Fe_{0.7}O_4$-RHC is used to activate PS to produce $SO_4^{\cdot-}$, $^{\cdot}OH$ and $^1O_2$ to decompose BPA into CO_2 and H_2O (eqn (44)). The mechanism of $ZnCo_{1.3}Fe_{0.7}O_4$-RHC activated PS to degrade BPA is shown in Fig. 14.

$$S_2O_8^{2-} + 2H_2O - 2e^- \rightarrow 2HSO_5^- + 2H^+ \quad (31)$$

$$Co^{3+} + HSO_5^- \rightarrow Co^{2+} + SO_5^{\cdot-} + H^+ \quad (32)$$

$$S_2O_8^{2-} + Co^{2+} \rightarrow Co^{3+} + SO_4^{2-} + SO_4^{\cdot-} \quad (33)$$

$$Fe^{3+} + H_2O \rightarrow FeOH^{2+} + H^+ \quad (34)$$

$$Co^{2+} + FeOH^{2+} \rightarrow CoOH^+ + Fe^{3+} \quad (35)$$

$$SO_4^{\cdot-} + H_2O \rightarrow HSO_4^- + {}^{\cdot}OH \quad (36)$$

$$Fe^{3+} + S_2O_8^{2-} \rightarrow Fe^{2+} + S_2O_8^{\cdot-} \quad (37)$$

$$Fe^{2+} + SO_4^{\cdot-}/{}^{\cdot}OH \rightarrow Fe^{3+} + SO_4^{2-}/OH^- \quad (38)$$

$$HSO_5^- \rightarrow H^+ + SO_5^{2-} \quad (39)$$

$$HSO_5^- + SO_5^{2-} \rightarrow SO_4^{2-} + HSO_4^- + {}^1O_2 \quad (40)$$

$$2SO_5^{\cdot-} + H_2O \rightarrow 3/2{}^1O_2 + 2HSO_4^- \quad (41)$$

$$2SO_5^{\cdot-} \rightarrow 2SO_4^{2-} + {}^1O_2 \quad (42)$$

$$2SO_5^{\cdot-} \rightarrow S_2O_8^{2-} + {}^1O_2 \quad (43)$$

$$SO_4^{\cdot-}/{}^{\cdot}OH/{}^1O_2 + BPA \rightarrow \text{intermediates} \rightarrow CO_2 + H_2O \quad (44)$$

4 Conclusions

In this study, a novel composite of $ZnCo_{1.3}Fe_{0.7}O_4$ spherical nanoparticles with primary particle size of about 13 nm interspersed on biological carbon base (RHC) was designed and prepared by solid phase method, using waste ferrous sulfate as the iron source. When used as a polyphase catalyst to activate PS to degrade BPA, the as-obtained $ZnCo_{1.3}Fe_{0.7}O_4$-50%RHC composite material could completely degrade BPA in 15 min, delivering better catalytic activity compared with the home-made $ZnCo_{1.3}Fe_{0.7}O_4$, $ZnFe_2O_4$ and $ZnCo_2O_4$. A series of experiment exploring the effects of several parameters and anions on BPA degradation demonstrated that the $ZnCo_{1.3}Fe_{0.7}O_4$-50%RHC possess excellent comprehensive performances including for PS activation. Stability and reusability tests substantiated that it still maintain excellent catalytic performance for BPA degradation after 5 cycles, and the leaching of metal ions is much lower than the discharge standard of wastewater. Based on free radical capture experiment, ESR test and XPS analysis, it is determined that there are free radical and non-radical pathways in the process of $ZnCo_{1.3}Fe_{0.7}O_4$-50%RHC activation of PS to degrade BPA. We believe that this "use waste to treat waste" idea and these findings provide an important guiding role for the development of magnetic separation catalyst for wastewater treatment process, as well as expand a new way with potential application prospect for the resource utilization of industrial by-product ferrous sulfate.

Authors contribution

Yirui Shu: conceptualization, data curation,fFormal analysis, methodology, software, validation, writing – original draft, writing – review & editing. Pan Zhang: investigation, visualization, software. Yanjun Zhong: writing – review & editing. Xiangyang Xu: writing – review & editing. Genkuan Ren: methodology, resources. Wei Wang: validation. Hengli Xiang: supervision. Zhiye Zhang: funding acquisition, investigation. Xinlong Wang: visualization, investigation, project administration.

Conflicts of interest

The authors declare that they have no known competing financial interests or personal relationships that could have appeared to influence the work reported in this paper.

Acknowledgements

This work was funded by the financial supported from Sichuan University-Panzhihua City Science and Technology Cooperation Special Fund for Titanium White by-product Ferrous Sulfate Preparation 500 tons/year Nanometer iron Red Pigment and Co-production Sulfuric Acid Pilot Study Project (No. 2018CDPZH-5) and Sichuan Provincial Science and Technology Planning Project (No. 2019YFH0149).

References

1 Y. Zhou, M. Chen, F. R. Zhao, D. Mu, Z. B. Zhang and J. Y. Hu, Ubiquitous occurrence of chlorinated byproducts of bisphenol A and nonylphenol in bleached food contacting papers and their implications for human exposure, *Environ. Sci. Technol.*, 2015, **49**, 7218–7226.

2 E. N. D. Freitas, G. A. Bubna, T. Brugnari, C. G. Kato, M. Nolli, T. G. Rauen, R. D. P. M. Moreira, R. A. Peralta and A. Bracht, Removal of bisphenol A and evaluation of ecotoxicity of degradation products by laccases from Pleurotus ostreatus, and Pleurotus pulmonarius, *Chem. Eng. J.*, 2017, **330**, 1361–1369.

3 E. J. Eio, M. Kawai, K. Tsuchiya, S. Yamamoto and T. Toda, Biodegradation of bisphenol A by bacterial consortia, *Int. Biodeterior. Biodegrad.*, 2014, **96**, 166–173.

4 C. M. Liu, Z. H. Diao, W. Y. Huo, L. J. Kong and J. J. Du, Simultaneous removal of Cu^{2+} and bisphenol A by a novel biocharsupported zero valent iron from aqueous solution: Synthesis, reactivity and mechanism, *Environ. Pollut.*, 2018, **239**, 698–705.

5 M. J. Xu, J. Li, Y. Yan, X. G. Zhao, J. F. Yan, Y. H. Zhang, B. Lai, X. Chen and L. P. Song, Catalytic degradation of sulfamethoxazole through peroxymonosulfate activated with expanded graphite loaded $CoFe_2O4$ particle, *Chem. Eng. J.*, 2019, **369**, 403–413.

6 D. Yang and C. M. Ezyske, Sulfate radical-advanced oxidation process (SR-AOP) for simultaneous removal of refractory organic contaminants and ammonia in landfill leachate, *Water Res.*, 2011, **45**, 6189–6194.

7 J. Wang and S. Wang, Activation of persulfate (PS) and peroxymonosulfate (PMS) and application for the degradation of emerging contaminants, *Chem. Eng. J.*, 2018, **334**, 1502–1517.

8 Y. C. Lee, S. L. Lo, P. T. Chiueh and D. G. Chang, Efficient decomposition of perfluorocarboxylic acids in aqueous solution using microwave-induced persulfate, *Water Res.*, 2009, **43**, 2811–2816.

9 X. Zhang, M. Feng, R. Qu, H. Liu, L. S. Wang and Z. Y. Wang, Catalytic degradation of diethyl phthalate in aqueous solution by persulfate activated with nano-scaled magnetic $CuFe_2O_4$/MWCNTs, *Chem. Eng. J.*, 2016, **301**, 1–11.

10 G. P. Anipsitakis and D. D. Dionysiou, Radical generation by the interaction of transition metals with common oxidants, *Environ. Sci. Technol.*, 2004, **38**, 3705–3712.

11 Y. Huang, C. Han, Y. Liu, M. N. Nadagouda, L. Machala, K. E. O Shea, V. K. Sharma and D. D. Dionysiou, Degradation of atrazine by $Zn_xCu_{1-x}Fe_2O_4$ nanomaterial-catalyzed sulfite under UV-vis light irradiation: Green strategy to generate $SO_4^{\bullet-}$, *Appl. Catal., B*, 2018, **221**, 380–392.

12 M. D. Hossain, M. N. Khan, S. Sikder, M. N. I. Khan and M. A. Hakim, Frequency and temperature dependent magnetic properties with structural Rietveld refinement of $Co_{0.25}Zn_{0.75}Y_xFe_{2-x}O_4$ ferrite, *J. Magn. Magn. Mater.*, 2020, **493**, 165696.

13 S. Debnath, D. Krishna and B. Saha, X-ray diffraction analysis for the determination of elastic properties of zinc-doped manganese spinel ferrite nanocrystals ($Mn_{0.75}Zn_{0.25}Fe_2O_4$), along with the determination of ionic radii, bond lengths, and hopping lengths, *J. Phys. Chem. Solids*, 2019, **134**, 105–114.

14 U. Wongpratat, P. Tipsawat, J. Khajonrit, E. Swatsitang and S. Maensir, Effects of Nickel and Magnesium on electrochemical performances of partial substitution in spinel ferrite, *J. Alloys Compd.*, 2020, **831**, 154718–154731.

15 H. Aali, N. Azizi, F. Kermani, M. Mashreghi, A. Youssefi, S. Mollazadeh, J. V. Khaki and H. Nasiri, High antibacterial and photocatalytic activity of solution combustion synthesized $Ni_{0.5}Zn_{0.5}Fe_2O_4$ nanoparticles: Effect of fuel to oxidizer ratio and complex fuels, *Ceram. Int.*, 2019, **45**, 19127–19140.

16 X. S. Rong, H. F. Chen, J. Rong, X. Y. Zhang, J. Wei, S. Liu, X. T. Zhou, J. C. Xu, F. X. Qiu and Z. R. Wu, An all-solid-state Z-scheme $TiO_2/ZnFe_2O_4$ photocatalytic system for the N_2 photofixation enhancement, *Chem. Eng. J.*, 2019, **371**, 286–293.

17 Q. R. Zhang, Z. W. Li, X. H. Li, L. G. Yu, Z. J. Zhang and Z. S. Wu, Zinc ferrite nanoparticle decorated boron nitride nanosheet: Preparation, magnetic field arrangement, and flame retardancy, *Chem. Eng. J.*, 2019, **356**, 680–692.

18 P. X. Liu, Y. M. Ren, W. J. Ma, J. Ma and Y. C. Du, Degradation of shale gas produced water by magnetic porous MFe_2O_4 (M = Cu, Ni, Co and Zn) heterogeneous catalyzed ozone, *Chem. Eng. J.*, 2019, **345**, 98–106.

19 J. N. Cui and H. L. Ren, Development and comparison of titanium dioxide production technology in China, *Rare Met. Cem. Carbides*, 2013, **41**, 14–17.

20 H. Q. Li, A brief analysis of 20 years development of titanium dioxide sulphuric acid process, *China Coat.*, 2019, **34**, 7–10.

21 S. Bi, Status and development of Titanium dioxide industry in China in 2018, *Iron, Steel, Vanadium, Titanium*, 2018, **39**, 1–4.

22 C. H. He, R. L. Shao and X. G. Liu, Progress in production technology of titanium dioxide, *Eng. Technol.*, 2016, **5**, 70–71.

23 Y. Wang, H. Sun, H. M. Ang, M. O. Tadé and S. Wang, Facile Synthesis of Hierarchically Structured Magnetic MnO_2/$ZnFe_2O_4$ Hybrid Materials and Their Performance in Heterogeneous Activation of Peroxymonosulfate, *ACS Appl. Mater. Interfaces*, 2014, **6**, 19914–19923.

24 X. Zhong, Z. S. Zou, H. L. Wang, W. Huang and B. X. Zhou, Enhanced Activation of Persulfate by Co-Doped Bismuth Ferrite Nanocomposites for Degradation of Levofloxacin Under Visible Light Irradiation, *Mater. Sci.*, 2019, **12**, 3952.

25 H. X. Zhang, C. W. Li, L. Lyu and C. Hu, Surface oxygen vacancy inducing peroxymonosulfate activation through electron donation of pollutants over cobalt-zinc ferrite for water purification, *Appl. Catal., B*, 2020, **270**, 1873–1883.

26 S. N. Divya and K. Manju, Heterogeneous catalytic oxidation of persistent chlorinated organics over cobalt substituted zinc ferrite nanoparticles at mild conditions: Reaction kinetics and catalyst reusability studies, *J. Environ. Chem. Eng.*, 2017, **5**, 964–974.

27 J. C. C. Freitas, M. A. Schettino, A. G. Cunha, F. G. Emmerich, A. C. Bloise and E. R. Azevedo, NMR investigation on the occurrence of Na species in porous carbons prepared by NaOH activation, *Carbon*, 2007, **45**, 1097–1104.

28 F. Y. Han, X. S. Xu, Y. S. Fu and X. Wang, Synthesis of Rice-Husk-Carbon-Supported Nickel Ferrite Catalyst for Reduction of Nitrophenols, *J. Nanosci. Nanotechnol.*, 2019, **19**, 5838–5846.

29 A. Arunkumar, D. Vanidha, R. Kannan and M. Shanmugam, Unusual Transition of Electrical and Magnetic Properties in the Nano to Bulk Transformation of Co-Zn Ferrites, *J. Supercond. Novel Magn.*, 2020, **33**, 1–15.

30 Y. Gong, D. Li, C. Luo, Q. Fu and C. Pan, Highly porous graphitic biomass carbon as advanced electrode materials for supercapacitors, *Green Chem.*, 2017, **19**, 4132–4140.

31 P. Laokul, V. Amornkitbamrung, S. Seraphin and S. Maensiri, Characterization and magnetic properties of nanocrystalline $CuFe_2O_4$, $NiFe_2O_4$, $ZnFe_2O_4$ powders prepared by the Aloe vera extract solution, *Curr. Appl. Phys.*, 2011, **11**, 101–108.

32 S. Patil, K. S. Anantharaju, D. Rangappa, Y. S. Vidya, S. C. Sharma, L. Renuka and H. Nagabhushana, Magnetic Eu-doped $MgFe_2O_4$ nanomaterials: An investigation of their structural, optical and enhanced visible-light-driven photocatalytic performance, *Environ. Nanotechnol. Monit. Manage.*, 2020, **13**, 100268.

33 Z. Shao, T. Zeng, Y. He, D. Zhang and X. Pu, A novel magnetically separable $CoFe_2O_4/Cd_{0.9}Zn_{0.1}S$ photocatalyst with remarkably enhanced H_2 evolution activity under visible light irradiation, *Chem. Eng. J.*, 2019, **359**, 485–495.

34 Y. Zhao, Y. Xu, J. Zeng, B. Kong, X. Geng, D. Li, X. Gao, K. Liang, L. Xu, J. Lian, S. Huang, J. Qiu, Y. Huang and H. Li, Low-crystalline mesoporous $CoFe_2O_4$/C composite with oxygen vacancies for high energy density asymmetric supercapacitors, *RSC Adv.*, 2017, **7**, 55513–55522.

35 C. J. Li, B. Y. Ma and X. X. Huo, Characterization of graphitization degree of carbon/carbon composites, *New Carbon Mater.*, 1999, **14**, 19–25.

36 W. Xiaobo, Q. Yanlei, Z. Lihua and T. Heqing, Nitrogen-Doped Reduced Graphene Oxide as a Bifunctional Material for Removing Bisphenols: Synergistic Effect between Adsorption and Catalysis, *Environ. Sci. Technol.*, 2015, **49**, 6855–6864.

37 M. Feng, Y. Liu, Z. Zhao, H. Huang and Z. Peng, The preparation of Fe doped triclinic-hexagonal phase heterojunction WO_3 film and its enhanced photocatalytic reduction of Cr (VI), *Mater. Res. Bull.*, 2019, **109**, 168–174.

38 S. Wang, J. Pu, Y. Tong, Y. Y. Cheng, Y. Gao and Z. H. Wang, $ZnCo_2O_4$ nanowire arrays grown on nickel foam for high-performance pseudocapacitors, *J. Mater. Chem. A*, 2014, **2**, 5434–5440.

39 M. M. Wang, H. H. Wu, C. R. Shen, S. P. Luo, D. Wang and L. He, Seaweed-like 2D-2D Architecture of MoS2/rGO Composites for Enhanced Selective Aerobic Oxidative Coupling of Amines, *Chemcatchem*, 2019, **7**, 1935–1942.

40 Z. Liu, S. Yang, Y. Yuan, J. Xu, Y. F. Zhu, J. J. Li and F. Wu, A novel heterogeneous system for sulfate radical generation through sulfite activation on a $CoFe_2O_4$ nanocatalyst surface, *J. Hazard. Mater.*, 2017, **324**, 583–592.

41 M. Kermani, F. Mohammadi and B. Kakavandi, Simultaneous catalytic degradation of 2,4-D and MCPA herbicides using sulfate radical-based heterogeneous oxidation over persulfate activated by natural hematite (α-Fe_2O_3/PS), *J. Phys. Chem.*, 2018, **117**, 49–59.

42 S. J. Olusegun, E. T. F. Freitas, L. R. S. Lara and N. D. S. Mohallem, Synergistic effect of a spinel ferrite on the adsorption capacity of nano bio-silica for the removal of methylene blue, *Environ. Technol.*, 2019, **45**, 1–33.

43 W. D. Oh and T. T. Lim, Design and application of heterogeneous catalysts as peroxydisulfate activator for organics removal: An overview, *Chem. Eng. J.*, 2019, **358**, 110–133.

44 J. Li, Y. Ren, F. Ji and B. Lai, Heterogeneous catalytic oxidation for the degradation of p -nitrophenol in aqueous solution by persulfate activated with $CuFe_2O_4$ magnetic nano-particles, *Chem. Eng. J.*, 2017, **324**, 63–73.

45 M. Li, Y. Xiong, X. Liu, X. Bo, Y. Zhang, C. Han and L. Guo, Facile synthesis of electrospun MFe_2O_4 (M = Co, Ni, Cu, Mn) spinel nanofibers with excellent electrocatalytic properties for oxygen evolution and hydrogen peroxide reduction, *Nanoscale*, 2015, **7**, 8920–8930.

46 S. Su, W. Guo, Y. Leng, C. L. Yi and Z. M. Ma, Heterogeneous activation of oxone by $Co_xFe_{3-x}O_4$ nanocatalysts for degradation of rhodamine B, *J. Hazard. Mater.*, 2013, **244**, 736–742.

47 C. Liang and H. W. Su, Identification of sulfate and hydroxyl radicals in thermally activated persulfate, *Ind. Eng. Chem. Res.*, 2009, **48**, 5558–5562.

48 M. Ahmadi, F. Ghanbari, A. Alvarez and S. S. Martinez, UV-LEDs assisted peroxymonosulfate/Fe^{2+} for oxidative removal of carmoisine: The effect of chloride ion, *Korean J. Chem. Eng.*, 2017, **34**, 1–8.

49 D. A. House, Kinetics and mechanism of oxidations by peroxydisulfate, *Chem. Rev.*, 1962, **62**, 185–203.

50 C. T. Chekem, S. Chiron, J. M. Mancaux, G. Plantard and V. Goetz, Thermal activation of persulfates for wastewater depollution on pilot scale solar equipment, *Sol. Energy*, 2020, **205**, 372–379.

51 W. Zhang, Z. Zhou, X. Shan, R. Xu, Q. Chen, G. He, X. Sun and H. Chen, Solvent-thermal preparation of $CuCo_2O_4$/RGO heterocomposite: an efficient catalyst for the reduction of p-nitrophenol, *New J. Chem.*, 2016, **40**, 4769–4774.

52 X. Lin, K. Shih, J. Chen, X. Xie, Y. L. Zhang, Y. Chen, Z. Chen and Y. Li, Insight into flower-like greigite-based peroxydisulfate activation for effective bisphenol A abatement: performance and electron transfer mechanism, *Chem. Eng. J.*, 2020, **391**, 123558.

53 X. B. Dong, B. X. Ren, Z. M. Sun, C. Q. Li, X. W. Zhang, M. H. Kong, S. L. Zheng and D. D. Dionysiou, Monodispersed $CuFe_2O_4$ nanoparticles anchored on natural kaolinite as highly efficient peroxymonosulfate catalyst for bisphenol A degradation, *Appl. Catal., B*, 2019, **253**, 206–217.

54 H. Lin, S. M. Li, B. Deng, W. H. Tan, R. M. Li, Y. Xu and H. Zhang, Degradation of bisphenol A by activating peroxymonosulfate with $Mn_{0.6}Zn_{0.4}Fe_2O_4$ fabricated from spent Zn-Mn alkaline batteries, *Chem. Eng. J.*, 2019, **364**, 541–551.

55 R. Yuan, S. N. Ramjaun, Z. Wang and J. Liu, Effects of chloride ion on degradation of Acid Orange 7 by sulfate radical-based advanced oxidation process: implications for formation of chlorinated aromatic compounds, *J. Hazard. Mater.*, 2011, **196**, 173–179.

56 Z. Wang, R. Yuan, Y. Guo, L. Xu and J. Liu, Effects of chloride ions on bleaching of azo dyes by Co^{2+}/oxone regent: Kinetic analysis, *J. Hazard. Mater.*, 2011, **190**, 1083–1087.

57 P. Villegas-Guzman, F. Hofer, J. Silva-Agredo and R. A. Torres-Palma, Role of sulfate, chloride, and nitrate anions on the degradation of fluoroquinolone antibiotics by photoelectro-Fenton, *Environ. Sci. Pollut. Res. Int.*, 2017, **24**, 1–15.

58 C. Tan, N. Gao, D. Fu, D. Jing and D. Lin, Efficient degradation of paracetamol with nanoscaled magnetic $CoFe_2O_4$ and $MnFe_2O_4$ as a heterogeneous catalyst of peroxymonosulfate, *Sep. Purif. Technol.*, 2017, **175**, 47–57.

59 Y. H. Guan, J. Ma, Y. M. Ren, Y. L. Liu, J. Y. Xiao, L. Q. Lin and C. Zhan, Efficient degradation of atrazine by magnetic porous copper ferrite catalyzed peroxymonosulfate oxidation via the formation of hydroxyl and sulfate radicals, *Water Res.*, 2013, **47**, 5431–5438.

60 X. Yu, J. Qu, Z. Yuan, P. Min, S. Hao, Z. Zhu, X. Li, D. Yang and Z. Yu, Anisotropic $CoFe_2O_4$@Graphene Hybrid Aerogels with High Flux and Excellent Stability as Building Blocks for Rapid Catalytic Degradation of Organic Contaminants in a FlowType Setup, *ACS Appl. Mater. Interfaces*, 2019, **11**, 34222–34231.

61 Q. Song, Y. Feng, Z. Wang, G. Liu and W. Lv, Degradation of triphenyl phosphate (TPhP) by $CoFe_2O_4$-activated peroxymonosulfate oxidation process: Kinetics, pathways, and mechanisms, *Sci. Total Environ.*, 2019, **681**, 331–338.

62 Z. Q. Yang, Y. Li, X. Y. Zhang, X. D. Cui, S. He, H. Liang and A. Ding, Sludge activated carbon-based $CoFe_2O_4$-SAC nanocomposites used as heterogeneous catalysts for degrading antibiotic norfloxacin through activating peroxymonosulfate, *Chem. Eng. J.*, 2020, **384**, 123319.

63 Y. Fan, Y. Zhou, Y. Feng, P. Wang, X. Y. Li and K. Shih, Fabrication of reactive flat-sheet ceramic membranes for oxidative degradation of ofloxacin by peroxymonosulfate, *J. Membr. Sci.*, 2020, **611**, 118302.

64 M. Xu, J. Li, Y. Yan, X. Zhao, J. Yan, Y. Zhang, B. Lai, X. Chen and L. Song, Catalytic degradation of sulfamethoxazole through peroxymonosulfate activated with expanded graphite loaded $CoFe_2O_4$ particles, *Chem. Eng. J.*, 2019, **369**, 403–413.

65 X. Duan, H. Sun and Y. Wang, N-Doping-Induced Nonradical Reaction on Single-Walled Carbon Nanotubes for Catalytic Phenol Oxidation, *ACS Catal.*, 2015, **5**, 553–559.

66 X. Q. Zhou, C. G. Luo, M. Y. Luo, Q. L. Wang, J. Wang, Z. W. Liao, Z. L. Chen and Z. Q. Chen, Understanding the synergetic effect from foreign metals in bimetallic oxides for PMS activation: A common strategy to increase the stoichiometric efficiency of oxidants, *Chem. Eng. J.*, 2020, **381**, 122587.

67 G. X. Huang, C. Y. Wang, C. W. Yang, P. C. Guo and H. Q. Yu, Degradation of bisphenol A by peroxymonosulfate catalytically activated with $Mn_{1.8}Fe_{1.2}O_4$ nanospheres: Synergism between Mn and Fe, *Environ. Sci. Technol.*, 2017, **51**, 12611–12618.

68 H. Fu, S. Ma, P. Zhao, S. Xu and S. Zhan, Activation of peroxymonosulfate by graphitized hierarchical porous biochar and $MnFe_2O_4$ magnetic nanoarchitecture for organic pollutants degradation: Structure dependence and mechanism, *Chem. Eng. J.*, 2019, **360**, 157–170.

69 W. Tian, H. Zhang, Z. Qian, T. Ouyang, H. Sun, J. Qin, M. O. Tadé and S. Wang, Bread-making synthesis of hierarchically Co@C nanoarchitecture in heteroatom doped porous carbons for oxidative degradation of emerging contaminants, *Appl. Catal., B*, 2018, **225**, 76–83.

70 H. Sun, X. Peng, S. Zhang, S. Liu, Y. Xiong, S. Tian and J. Fang, Activation of peroxymonosulfate by nitrogen-functionalized sludge carbon for efficient degradation of organic pollutants in water, *Bioresour. Technol.*, 2017, **241**, 244251.

